Journal of Computational Science 83 (2024) 102453

Contents lists available at ScienceDirect

Journal of Computational Science

journal homepage: www.elsevier.com/locate/jocs

A numerical framework for modeling evaporation and combustion of isolated, spherically-symmetric, multi-component fuel droplets

Alberto Cuoci [a,*], Edoardo Cipriano [a], Abd Essamade Saufi [a,b], Alessio Frassoldati [a]

[a] Department of Chemistry, Materials, and Chemical Engineering "G. Natta", Politecnico di Milano, Italy
[b] First Light Fusion Ltd., Unit 9/10, Oxford Pioneer Park, Mead Road, Oxford, OX5 1QU, Oxfordshire, United Kingdom

ARTICLE INFO

Dataset link: https://www.opensmokepp.polimi.it

Keywords:
Droplet
Microgravity
Autoignition
Evaporation
Cool flame

ABSTRACT

This paper presents a comprehensive numerical framework for simulating the evaporation and combustion of isolated, spherically-symmetric, multi-component fuel droplets. The framework incorporates a detailed description of chemical reactions in the gaseous phase and is capable of modeling pure evaporation, autoignition, and hot-wire ignition scenarios.

The transport equations for mass, species, and energy are solved in both the liquid (droplet) and gaseous (surrounding atmosphere) phases. Diffusion in the liquid phase is described using the Stefan–Maxwell theory, while in the gaseous phase, both molecular and thermal diffusion are considered. The model also includes the thermophoretic effect for carbonaceous particles and accounts for gas radiation through various models, ranging from optically-thin approximations to more complex methods like the P1 and discrete ordinate methods. Non-gray radiative effects are handled using the Weighted-Sum-of-Gray-Gases Model (WSGGM). Liquid/gas interface conditions are evaluated by imposing flux continuity of mass and energy, along with thermodynamic equilibrium for species. Deviations from ideal thermodynamic behavior in the liquid droplet are managed by incorporating a suitable activity coefficient or by using a proper cubic equation of state. Additionally, the presence of supporting fibers is modeled using a simplified one-dimensional approach. The transport equations are solved using the method of lines, with spatial discretization performed via the finite difference method on a body-fitted grid. The resulting system of Differential–Algebraic Equations (DAEs) is then solved using a fully-coupled approach.

Thanks to its generality in terms of kinetic and thermodynamic descriptions and the reduced computational time, the proposed framework offers significant potential for advancing our understanding of the complex combustion processes of multi-component liquid fuels and for enhancing the planning and execution of experiments involving isolated fuel droplets.

1. Introduction

The combustion of liquid fuels is of great interest for many practical applications, such as industrial burners and internal combustion engines, particularly due to their high energy density per unit volume [1]. In most devices, liquid fuel is injected into the combustion chamber as an intermittent or continuous spray of small droplets (sub-millimeter size). Combustion requires evaporation of fuel droplets and proper mixing of vaporized fuel with air. Good combustion conditions typically occur when the fuel burns in premixed and prevaporized mode (for example in premixed turbine engines, homogeneous charge engines, compression ignition engines, etc.), or at least in a *mixed* mode (for example in gasoline direct injection engines) [2].

The strong interactions between the many physico-chemical processes (evaporation, mixing, chemical reactions, turbulence, etc.) dominating the combustion of fuel droplets make the study of spray combustion a very complex subject, on both the experimental and modeling/numerical sides [3]. Thus, it is useful to take apart the overall system and to study simpler and possibly ideal conditions. A first simplification consists in considering an isolated fuel droplet with a surrounding volume of gas. Such a system includes all of the existing basic processes occurring in practical combustors: heat-up, evaporation, diffusion, and combustion (i.e. chemical reactions). In addition, the introduction of spherical symmetry further simplifies the system: only one spatial dimension enters the description of the evaporation/combustion process, so that the 1D, time-dependent transport equations apply [4,5].

* Corresponding author.
E-mail address: alberto.cuoci@polimi.it (A. Cuoci).

https://doi.org/10.1016/j.jocs.2024.102453
Received 28 June 2024; Received in revised form 2 September 2024; Accepted 3 October 2024
Available online 9 October 2024

This greatly facilitates both computational and theoretical descriptions of the problem [2,6,7], improving our understanding of experimental results, which would be much more difficult and less accurate in multidimensional conditions [8]. In particular, since only 1D transport equations are solved, we can expect a significant reduction (with respect to the general 3D case) of computational time and memory requirements, especially when complex kinetic mechanisms are adopted for describing the combustion reactions.

Obviously, in normal gravity, isolated droplets of the sizes typically studied experimentally (~1 mm) cannot be considered perfectly spherical, and natural convection destroys the spherical symmetry of the combustion process, as evident in the earliest experiments carried out on isolated fuel droplets [9,10]. However, smaller droplets should maintain spherical symmetry due to the low Grashof number, especially at atmospheric pressure, making the use of a 1D model a reasonable approximation in such cases. Ideal spherical-symmetric conditions can be approached only via reduced-gravity (or microgravity) experiments. Depending on the droplet size, microgravity conditions are attained through drop towers, parabolic trajectories, or in space-based experiments [1,11]. These experiments have revealed important phenomena in droplet burning, such as radiative flame extinction, disruptive burning, and the formation of cool flames. In particular, the longer observation times available in space-based experiments provided the opportunity to investigate phenomena such as: formation of stable cool flames [12,13], transition from diffusive to radiative extinction [14], departures from quasi-steady combustion, formation of soot shells around the droplets [15–17], etc. Although typical sizes of droplets adopted in microgravity experiments are significantly larger than those of droplets in sprays, they provide fundamental information on the intricate coupling between the physical and chemical processes involved. In fact, as mentioned before, they represent an optimal compromise between the complexity of the problem and its completeness, since most of the phenomena involved in the combustion of real sprays are still accounted for. In this way, the physical sub-models representing each of them (thermodynamics, radiation, chemical reactions, etc.) can be evaluated in a relatively *simplified* context. On the contrary, to evaluate the theoretical models of governing phenomena from the interpretation of multidimensional experiments would be much more complicated, due to the resulting physical (and therefore modeling/numerical) complexity [18].

The reduced computational cost of 1D simulations, due to spherical symmetry, enables detailed modeling of chemical reactions, radiative heat transfer, and non-ideal thermodynamics. In particular, the adoption of detailed kinetic mechanisms (hundreds of chemical species and thousands of reactions), also including low-temperature oxidation mechanisms, is strictly necessary to numerically estimate the ignition delay times, the explosion diagrams and to correctly model the formation of pollutant species, such as NOx, SOx, unburned and poly-aromatic hydrocarbons (PAH) and carbonaceous particles (soot). More in general, complex kinetics is needed also to better understand observed non-conventional burning rates under specific conditions. As an example, recent Flame Extinguishment Experiments (FLEX) [8], carried out by NASA on hot-wire ignited, isolated fuel droplets of large n-alkanes onboard the International Space Station (ISS), revealed the existence of a new, complex phenomenon, where a hot flame extinction leads to the formation of a stable low-temperature *cool flame* [12,19]. As demonstrated by recent works on combustion of droplets in reduced gravity, non-luminous radiation from species such as CO, CO_2 and H_2O can have a significant effect on phenomena which are highly sensitive to the flame temperature. In particular, radiative heat loss reduces the burning rate of larger droplets and promotes the so-called radiative flame extinction. Obviously, the effect of radiation in droplet flames fundamentally differs from its effect on gaseous planar flames, so it is important to include a proper radiative heat transfer model accounting for the spherical geometry of the combustion process. The characterization of equilibrium thermodynamics at the liquid/gas interface is crucial for a correct prediction of vaporization rates, especially for non-ideal mixtures and high pressure cases. As an example, recent numerical simulations demonstrated that vaporization of n-heptane and n-decane droplets at high pressure (up to 50 atm) can be correctly captured only through proper account of non-unitary fugacity coefficients and Poynting correction [20].

In this work, we present a numerical framework for the transient modeling of evaporation and combustion of spherically-symmetric, isolated multi-component fuel droplets. The code, which is built on top of the `OpenSMOKE++` platform [21], is specifically conceived for including a detailed description of combustion reactions, through detailed kinetic mechanisms with hundreds of species. The code is able to model pure evaporation, autoignition, and spark- or hot-wire-ignition cases. The transport equations of mass, species and energy are solved in the liquid and gaseous phase. Liquid/gas interface conditions are evaluated by imposing flux continuity of mass and energy and thermodynamic equilibrium for species. Diffusion in the gaseous phase includes molecular (Fick's law), thermal (Soret effect) and thermophoretic (for carbonaceous particles only) contributions. Detailed description of diffusion in the liquid phase (in case of multi-component droplets) is carried out through the Stefan–Maxwell theory. Detailed thermodynamics in the gaseous phase is included, based on Peng–Robinson equation of state for the evaluation of the compressibility factor and fugacity coefficients. Deviations from the ideal thermodynamic behavior in the liquid droplet are accommodated by introducing a proper activity coefficient or a proper cubic equation of state. Gas radiation is described through several models, with increasing levels of accuracy (optically-thin, analytical solution for a gray gas between concentric spheres, P1, and discrete ordinate methods). Non-gray radiative effects are modeled in a simplified way through the Weighted-Sum-of-Gray-Gases Model (WSGGM), which represents a satisfactory compromise between accuracy and complexity (and hence computational cost). The presence of one or more fibers can be simulated using the simplified approach proposed by Farouk and Dryer [22]. The solution of transport equations is based on the method of lines. The spatial discretization is carried out by means of the finite difference method (using a non-uniform, body-fitted grid) and the resulting DAE (Differential–Algebraic Equations) system is solved using a fully-coupled approach.

The manuscript is organized as follows. In Section 2, the mathematical model is presented. In particular, we show in detail the governing transport equations in both the liquid and gaseous phase, the liquid/gas interface conditions, and the equations for all the relevant sub-models (such as radiative heat transfer). In Section 3, the numerical methodology adopted for solving the discretized system of equations is described. In Section 4, we present several examples of possible applications of the framework, focusing on three classes of problems: pure evaporation, auto-ignition and hot-wire-ignition of isolated single- or multi-component droplets. The paper concludes with a discussion about the future work and possible extensions.

2. Mathematical model

The mathematical model describes the combustion of an isolated fuel droplet in a gas-phase environment, in spherical-symmetric conditions (idealizing the reduced-gravity experimental conditions associated to drop towers, parabolic trajectories and space-based experiments). The main following assumptions are taken into account:

- spherical symmetry and absence of natural convection effects;
- constant pressure;
- absence of reactions in liquid phase;
- thermodynamic equilibrium at the liquid/gas interface.

In particular, the spherical symmetry allows to model the droplet-gas system with 1-dimensional equations.

2.1. Liquid phase equations

In case of a single-component liquid droplet, the mass and energy transport equations in the liquid phase are:

$$\frac{\partial \rho_L}{\partial t} + \frac{1}{r^2}\frac{\partial}{\partial r}\left(r^2 \rho_L v_L\right) = 0 \tag{1}$$

$$\rho_L c_{p,L}\left(\frac{\partial T_L}{\partial t} + v_L \frac{\partial T_L}{\partial r}\right) = \frac{1}{r^2}\frac{\partial}{\partial r}\left(r^2 k_L \frac{\partial T_L}{\partial r}\right) + S_L^f \tag{2}$$

where the subscript L denotes the liquid phase. ρ is the density, v the convective velocity, c_p the constant-pressure specific heat and k the thermal conductivity. S_L^f is the heat gain to the liquid phase due to the possible presence of one or more supporting fibers (see Section 2.9).

In case of multi-component droplets, additional equations for the conservation of species are added:

$$\rho_L\left(\frac{\partial Y_{L,i}}{\partial t} + v_L \frac{\partial Y_{L,i}}{\partial r}\right) = -\frac{1}{r^2}\frac{\partial}{\partial r}\left(r^2 j_{L,i}^d\right) \qquad i = 1, \dots, NL \tag{3}$$

and the energy transport equation is modified into:

$$\rho_L c_{p,L}\left(\frac{\partial T_L}{\partial t} + v_L \frac{\partial T_L}{\partial r}\right) = \frac{1}{r^2}\frac{\partial}{\partial r}\left(r^2 k_L \frac{\partial T_L}{\partial r}\right) - \sum_i j_{L,i}^d c_{p,L,i}\frac{\partial T_L}{\partial r} + S_L^f \tag{4}$$

In the equations reported above, $j_{L,i}^d$ is the liquid-phase diffusion flux of species ith evaluated on the basis of the Stefan–Maxwell theory, according to what described in Section 2.5.1. $c_{p,L,i}$ is the constant-pressure specific heat of species ith in the liquid phase. Thermodynamic and transport properties of individual liquid-phase species are assumed temperature-dependent and evaluated through the correlations available in the Yaws' database [23,24].

2.2. Gas phase equations

Similarly, for the gaseous phase, the following mass, energy and species conservation equations are written:

$$\frac{\partial \rho_G}{\partial t} + \frac{1}{r^2}\frac{\partial}{\partial r}\left(r^2 \rho_G v_G\right) = 0 \tag{5}$$

$$\rho_G c_{p,G}\left(\frac{\partial T_G}{\partial t} + v_G \frac{\partial T_G}{\partial r}\right) = \frac{1}{r^2}\frac{\partial}{\partial r}\left(r^2 k_G \frac{\partial T_G}{\partial r}\right) + - \sum_i j_{G,i}^d c_{p,G,i}\frac{\partial T_G}{\partial r} - \sum_{i=1}^{NS} \dot{\Omega}_{G,i}\hat{h}_{R,i} - \nabla \dot{q}_R + S_G^f \tag{6}$$

$$\rho_G\left(\frac{\partial Y_{G,i}}{\partial t} + v_G \frac{\partial Y_{G,i}}{\partial r}\right) = = -\frac{1}{r^2}\frac{\partial}{\partial r}\left(r^2\left(j_{G,i}^d + j_{G,i}^s + j_{G,i}^{th}\right)\right) + \dot{\Omega}_{G,i} \qquad i = 1, \dots, NS \tag{7}$$

where the subscript G indicates gas-phase properties. Considering the ith gas-phase species, $Y_{G,i}$ is its mass fraction, $j_{G,i}^d$ is its gas-phase diffusion flux evaluated through the Fick's law, $j_{G,i}^s$ is its flux generated by Soret effect, $j_{G,i}^{th}$ is its flux due to thermophoresis (cfr. Section 2.6), $\dot{\Omega}_{G,i}$ is its formation rate: $\dot{\Omega}_{G,i} = \sum_{j=1}^{NR} \nu_{ij} r_j$, with r_j being the rate of the jth reaction (NS and NR are respectively the total number of species and reactions). $\hat{h}_{R,i}$ is the mass enthalpy of formation of the ith species and finally $\dot{q}_R$ is the radiative heat flux (cfr. Section 2.7). Diffusiophoretic and photophoretic effects are here neglected, although a minor influence on soot formation had been hypothesized in previous works [25,26]. S_G^f is the heat gain to the gaseous phase due to the possible presence of one or more supporting fibers (see Section 2.9).

2.3. Liquid/gas interface equations

Liquid/gas interface is described by imposing continuity of mass and energy fluxes, continuity of temperature, and thermodynamic equilibrium for species:

$$\dot{m}_v Y_{L,i} - j_{L,i}^d = \dot{m}_v Y_{G,i} - j_{G,i}^{tot} \qquad i = 1, \dots, NL \tag{8}$$

$$k_L \left.\frac{\partial T_L}{\partial r}\right|_{R_d} + \sum_{i=1}^{NL}\left(\dot{m}_v Y_{G,i} + j_{G,i}^{tot}\right)\Delta\hat{h}_{v,i} = k_G \left.\frac{\partial T_G}{\partial r}\right|_{R_d} + \dot{q}_{rad}^{surf} \tag{9}$$

$$T_L\big|_{R_d} = T_G\big|_{R_d} \tag{10}$$

$$f_{L,i}\big|_{R_d} = f_{G,i}\big|_{R_d} \qquad i = 1, \dots, NL \tag{11}$$

where R_d is the radius of the droplet, $\Delta\hat{h}_{v,i}$ the vaporization enthalpy of species ith, $\dot{q}_{rad}^{surf}$ is the radiative heat flux on the droplet surface, and $f_{L,i}$ and $f_{G,i}$ are the fugacities of species ith in the liquid and gaseous phases, respectively. The vaporization flux $\dot{m}_v$ is given by:

$$\dot{m}_v = \rho_G\left(v_G - \frac{dR_d}{dt}\right) \tag{12}$$

2.4. Boundary conditions

Symmetry conditions are imposed in the center of the droplet $r = 0$:

$$v_L\big|_0 = 0 \tag{13}$$

$$\left.\frac{\partial T_L}{\partial r}\right|_0 = 0 \tag{14}$$

$$\left.\frac{\partial Y_{L,i}}{\partial r}\right|_0 = 0 \qquad i = 1, \dots, NL \tag{15}$$

At the outer boundary R_∞ (~100 times the droplet radius), Neumann's boundary conditions are typically imposed:

$$\left.\frac{\partial v_G}{\partial r}\right|_{R_\infty} = 0 \tag{16}$$

$$\left.\frac{\partial T_G}{\partial r}\right|_{R_\infty} = 0 \tag{17}$$

$$\left.\frac{\partial Y_{G,i}}{\partial r}\right|_{R_\infty} = 0 \qquad i = 1, \dots, NS \tag{18}$$

2.5. Diffusion fluxes

2.5.1. Liquid phase

Diffusion fluxes are described through Stefan–Maxwell theory [27]. Differently from a Fick-based approach, the diffusion flux of the ith species depends on the composition of the overall mixture. In radial coordinates, molar diffusion fluxes $\mathbf{J}_L$ are then calculated by solving the linear system:

$$\mathbf{J}_L \cdot \mathbf{B} = -c_{L,tot}\boldsymbol{\Gamma}\frac{\partial \mathbf{x}}{\partial r} \tag{19}$$

where $c_{L,tot}$ is the liquid-phase concentration, $\frac{\partial \mathbf{x}}{\partial r}$ is the radial gradient of molar fractions. The $\mathbf{B}$ matrix is evaluated as:

$$\begin{cases} B_{ik} = -x_i\left(\frac{1}{\Lambda_{ik}} - \frac{1}{\Lambda_{in}}\right) & i \neq k \\ B_{ii} = \frac{x_i}{\Lambda_{in}} + \sum_{j\neq i}^{n}\frac{x_j}{\Lambda_{ij}} \end{cases} \tag{20}$$

where Λ_{ij} is the Stefan–Maxwell binary diffusion coefficient, calculated following Wesselingh and Krishna [28]:

$$\Lambda_{ij} = \left(\Lambda_{ij}^0\right)^{(1+x_j-x_i)/2} \cdot \left(\Lambda_{ji}^0\right)^{(1+x_i-x_j)/2} \tag{21}$$

Λ_{ij}^0th is the infinite dilution diffusion coefficient of the ith species into j, which can be evaluated through the Siddiqi–Lucas correlation [29], for example, for both polar and non-polar systems. $\boldsymbol{\Gamma}$ is the activity matrix, whose elements are defined as:

$$\Gamma_{ij} = \delta_{ij} + x_i\left(\frac{\partial \ln \gamma_i}{\partial x_j}\right)_{T,P,x_{k\neq j=1\dots NL-1}} \tag{22}$$

where γ_i is the ith activity coefficient, evaluated through a UNIFAC approach [30]. Note that $\mathbf{J}_L$, $\mathbf{B}$ and $\boldsymbol{\Gamma}$ are of order $NL - 1$, because

the NLth diffusion flux is not independent, and is evaluated through flux closure:

$$J_{NL} = -\sum_{i=1}^{NL-1} J_i \tag{23}$$

Species NL is locally chosen as the species with the largest mole fraction. Molar fluxes $\mathbf{J}_L$ are then converted into mass fluxes $\mathbf{j}_L$ [27] to make them homogeneous into Eqs. (3) and (4).

2.5.2. Gas phase

The diffusion fluxes are expressed as a function of the corresponding diffusion velocities. In particular for the gaseous phase, the three fluxes appearing in Eq. (7) becomes:

$$j^d_{G,i} + j^s_{G,i} + j^{th}_{G,i} = \rho_G Y_{G,i}\left(V^d_{G,i} + V^s_{G,i} + V^{th}_{G,i}\right) \tag{24}$$

In the expression above, the molecular $V^d_{G,i}$ and thermal $V^s_{G,i}$ diffusion velocities are given by:

$$V^d_{G,i} = -\frac{\Gamma_{G,i}}{Y_{G,i}}\frac{\partial Y_{G,i}}{\partial r} \tag{25}$$

$$V^s_{G,i} = -\frac{\Gamma_{G,i}\Theta_{G,i}}{X_{G,i}}\frac{1}{T_G}\frac{\partial T_G}{\partial r} \tag{26}$$

where $X_{G,i}$ is the mole fraction and $\Theta_{G,i}$ the thermal diffusion ratio of species ith. The thermal diffusion ratios are estimated according to the theory of non-uniform gases [31]. $\Gamma_{G,i}$ is the Fick's individual species mixture averaged diffusion coefficient, related to the binary diffusion coefficients $\Gamma_{G,ji}$ through the expression:

$$\Gamma_{G,i} = \frac{1 - Y_{G,i}}{\sum_{j\neq i}\frac{X_{G,i}}{\Gamma_{G,ji}}} \tag{27}$$

The contribution due to the pressure-gradient diffusion was neglected for all the simulations analyzed in this work. Indeed, the pressure-gradient contribution plays a very marginal role in the numerical modeling of conventional laminar flames and it is usually ignored [32]. The approach proposed by Coffee and Heimerl [33] is adopted to enforce the mass conservation. This approach is based on a so-called correction diffusion velocity V_C, which is defined as:

$$V^C_{G,i} = V_{G,i} + V_C \tag{28}$$

where V_C is a constant correction factor, independent of species (but varying in space and time). This correction factor is introduced to satisfy the mass conservation and is evaluated as:

$$V_C = -\sum_{i=1}^{NS} Y_{G,i} V_{G,i} \tag{29}$$

The Fick's law (together with the light species approximation for the evaluation of the thermal diffusion ratios) could lead to some inaccuracies. In such cases, a full multicomponent approach should be adopted in order to improve the accuracy and enforce the conservation of mass without additional corrections [34]. The application of full multicomponent transport models is computationally very expensive and the computational cost increases at least with the square of the number of the transported species.

2.6. Thermophoretic effect

The thermophoretic effect on particles produced by the combustion process is included in the model. The thermophoretic velocity is given by the following general expression [35]:

$$v_{th} = -V_{th,r}\frac{\mu_G}{\rho_G}\frac{\nabla T_G}{T_G} \tag{30}$$

where μ_G is dynamic viscosity , T_G is temperature, and $V_{th,r}$ is the thermophoretic diffusivity (or reduced thermophoretic velocity). Stagni et al. [18] provided an extensive discussion about the estimation of such a thermophoretic diffusion and compared different theoretical model and assumptions. As far as soot particles are concerned, the description is particularly complex, because thermophoretic velocities depend on primary particle sizes because of the open structure of the aggregates. A default value of $V_{th,r} \approx 0.538$ is assumed.

2.7. Radiation

The gas-phase transport Eq. (6) accounts for the radiation contributions from non-luminous gases (mainly CO_2 and H_2O) and luminous soot particles via the $\nabla\dot{q}_R$ term. Considering a gray medium, the divergence of radiative heat flux is evaluated as [36]:

$$\nabla\dot{q}_R = \kappa\left(4\pi I_b - \int_{4\pi} I\, d\Omega\right) \tag{31}$$

where κ is the Planck mean absorption coefficient, I_b is the blackbody intensity $I_b = \sigma T^4/\pi$ (σ is the Stefan–Boltzmann constant) and I is the radiation intensity. Different approaches, with different levels of accuracy and complexity, are available to model I: the optically-thin model, the analytical solution proposed by Viskanta and Merriam [37], the P1 radiation model and the Discrete Ordinates Model (DOM). In particular, the P1 model represent a good compromise between computational load and accuracy. The interested reader can easily found the details of the radiative heat transfer models cited above in the existing literature [36]. A more critical aspect is represented by the modeling of the mean absorptivity, due to the non-gray behavior of CO_2 and H_2O, and to the major role of soot radiation. A convenient way to represent a nongray medium consists in using a Weighted-Sum-of-Gray-Gases Model (WSGGM) [38]. With this methodology, a number of equivalent gray gases are used for each medium, weighted through temperature-dependent factors. These are obtained via polynomial fitting procedures with experimental measurements:

$$\omega_k = \sum_{j=1}^{J} b_{k,j} T^{j-1} \tag{32}$$

where T is the gas temperature and $b_{k,j}$ are the polynomial fitting coefficients. The combination between $N_g + 1$ and N_s equivalent gray gases (for absorbing gases and soot, respectively) produces $\left(N_g + 1\right) \times N_s$ total gray gases. Indeed, a transparent window must be considered for CO_2/H_2O, i.e. $\kappa_{g,0} = 0$. For each (n,m) gray gas the combined absorption coefficient can be evaluated as:

$$\kappa_{n,m} = \kappa_{s,n} + P\kappa_{g,m} \tag{33}$$

where P is the pressure. The combined (n,m) weighting factor is obtained through the product of the weighting factors:

$$\omega_{n,m} = \omega_n \omega_m \tag{34}$$

Once the coefficients have been calculated, one Eq. (31) is solved for each gray gas [38,39]:

$$\nabla\dot{q}_{R,n,m} = \kappa_{n,m}\left(4\pi\omega_{n,m} I_b - \int_{4\pi} I_{n,m} d\Omega\right) \tag{35}$$

then summing up the respective contributions to obtain $\nabla\dot{q}_R$. A critical point in the development of WSGG models consists in the parameters estimation for the equivalent gray gases: usually, this is done through fitting procedures [40,41] for mixtures with fixed H_2O/CO_2 ratios, and separately for soot [42]. More specifically, we use the novel procedure developed by Cassol et al. [43] to estimate coefficients for arbitrary compositions of H_2O, CO_2 and soot. Considering the time- and space-variable composition of the gas-phase environment, Cassol's model is thus able to guarantee the needed flexibility in managing the radiative contribution to the energy balance (6), without compromising computational efficiency.

2.8. Thermodynamic equilibrium

As mentioned in Section 1, a proper description of thermodynamic equilibrium at the liquid/gas interface is of significant relevance for the correct estimation of vaporization/burning rates of droplets. The task is particularly challenging in case of deviations from the ideal-gas behavior in the gaseous phase at high pressure and especially in case of non-ideal effects in a multicomponent droplet.

In particular, for the liquid phase the fugacity $f_{L,i}$ of species ith at the interface, is evaluated according to:

$$f_{L,i} = p_i^0 X_{L,i} \phi_{L,i} e^{\int_{p_i^0}^{p} \frac{v_{L,i}}{RT} dp} \gamma_j \tag{36}$$

In the expression above, p_i^0 is the partial pressure of species ith at the interface temperature, $X_{L,i}$ its molar fraction, $\phi_{L,i}$ its gas-phase fugacity coefficient for the pure species and γ_j its activity coefficient in the liquid mixture. The $e^{\int_{p_i^0}^{p} \frac{v_{L,i}}{RT} dp}$ term represents the so-called Poynting's correction, where $v_{L,i}$ is the liquid molar volume of the pure species. In case of a single-component droplet, the activity coefficient is by definition equal to 1.

For the gaseous phase, the fugacity $f_{G,i}$ of species ith at the interface is evaluated according to:

$$f_{G,i} = p Y_{G,i} \phi_{G,i}^{mix} \tag{37}$$

where p is the total pressure, $Y_{G,i}$ the mass fraction of species ith and $\phi_{G,i}^{mix}$ its fugacity coefficient in the gas-phase mixture.

The fugacity coefficients appearing in Eqs. (36) and (37) are estimated through the Peng–Robinson cubic equation of state [44], while the activity coefficients γ_j for multicomponent liquid mixtures through the UNIFAC approach [45].

2.9. Fiber model

Supporting fibers are modeled using the 1D model proposed by Farouk and Dryer [22]. The temperature distribution in the fiber can be assumed to be 1D, since the typical diameter of supporting fibers is much smaller (ranging from 10 to 150 μm) than droplet diameters considered in experiments and the Biot numbers are of the order of $o(10^{-2})$. If we neglect the interaction with radiative heat transfer, the energy equation along the fiber can be written as:

$$\frac{\partial}{\partial t}\left(\rho_f Cp_f T_f\right) = \frac{\partial}{\partial r}\left(k_f \frac{\partial T_f}{\partial r}\right) + \frac{4h_\infty}{d_f}\left(T_{L/G} - T_f\right) \tag{38}$$

where T_f is the fiber temperature, ρ_f is the fiber density, Cp_f is the specific heat of the fiber, k_f is the fiber thermal conductivity, d_f is the fiber diameter and h_∞ is the heat transfer coefficient. $T_{L/G}$ is the temperature of liquid or gaseous phase, according to the radial coordinate.

We assume the fiber as a horizontal cylinder and we evaluate the heat transfer coefficient as $h_\infty = Nu_\infty k_\infty / d_f$. k_∞ is the thermal conductivity of liquid or gaseous phase (depending on the radial coordinate r, i.e. if the fiber is immersed in the droplet or in the gaseous atmosphere, respectively).

The Nusselt number is $Nu_\infty = 0.36$ in case of limiting stagnant situation [46]. More accurate correlations can be adopted, which are valid for low Reynolds number flows, such as the correlations of Andrews et al. [47] $Nu_\infty = (0.34 + 0.65 Re_{d_f}^{0.45})$ and Collis and Williams [48] $Nu_\infty = (0.24 + 0.56 Re_{d_f}^{0.45})\left(\frac{T_\infty + T_f}{2T_\infty}\right)$.

The heat flux from the fiber to the liquid or gaseous phase $q_{L/G}^f$ can be easily estimated once the fiber temperature T_f is available:

$$q_{L/G}^f = \frac{4h_\infty}{d_f}\left(T_f - T_{L/G}\right) \tag{39}$$

Finally, the heat gain terms S_L^f and S_G^f appearing in the energy transport Eqs. (4) and (6) are calculated as:

$$S_{L/G}^f = n_f q_{L/G}^f \frac{d_f^2}{16 r^2} \tag{40}$$

where n_f is the number of fibers and r is the radial coordinate.

2.10. Internal recirculations

The model assumes spherical symmetry within the liquid and gaseous phases, which simplifies the computational approach and maintains feasibility for fully-coupled simulations involving complex chemistry and phase interactions. However, it is recognized that internal recirculations within the droplet can play a significant role during the evaporation and combustion processes [6,49], particularly under certain conditions such as during ignition or in fiber-supported tests.

While the adopted spherically-symmetric formulation cannot explicitly account for these effects, it is possible to approximate the impact of liquid-phase motion through modifications to the effective transport properties. One potential approach consists in introducing corrective terms or effective diffusivities that account for the enhanced mixing due to internal circulation within the droplet [6,50]. These modifications could be guided by empirical correlations or simplified models of internal liquid motion, which would allow the model to better capture the effects of liquid-phase dynamics without requiring a full multi-dimensional treatment.

The framework is already designed to accommodate user-defined modifications to the transport properties. This feature allows users to artificially adjust transport coefficients to simulate the effects of internal circulation or other complex liquid-phase dynamics. By modifying these transport properties, users can emulate the enhanced mixing and altered diffusion characteristics that would result from internal liquid-phase motion. This flexibility provides a practical way to approximate these effects without the need for a fully multi-dimensional treatment.

2.11. Initial conditions

The initial temperature profile in the gas phase differs according to the type of experiment to be modeled. In the case of autoignition, a uniform temperature profile is assumed.

Hot-wire- or spark-ignition experiments, on the other hand, require a more complex description. To enforce the ignition, a temperature profile peaking at ~2200–2500 K is imposed as initial condition in the proximity of the liquid interface, according to what reported in Fig. 1. Although in experimental devices the spark- or hot-wire-ignition might in principle compromise the spherical symmetry, this effect is neglected in this model, as already done in previous works [50,51].

3. Numerical algorithm

The overall model consists of a system of partial differential equations for the liquid (Eqs. (1), (3) and (4)) and gaseous (Eqs. (5) to (7)) phases. The two sets of equations share the liquid/gas droplet surface, where proper interface conditions are prescribed (Eqs. (8) to (11)). Boundary conditions defined at the droplet center (Eqs. (13) to (15)) and at the outer radius of the gaseous phase surrounding the droplet (Eqs. (16) to (18)). The partial differential equations are numerically solved through the method of lines, which consists in discretizing the spatial derivatives only, leaving the time variable continuous. In particular, the spatial discretization, based on the Finite Difference Method (FDM), is applied on a 1D moving spatial mesh (see below). The convective terms appearing in the governing equations are discretized using the first-order upwind discretization, while the second derivatives associated to the conduction/diffusion terms are discretized using a second-order centered scheme. The continuity equation receives a special treatment compared to other transport equations. Since pressure

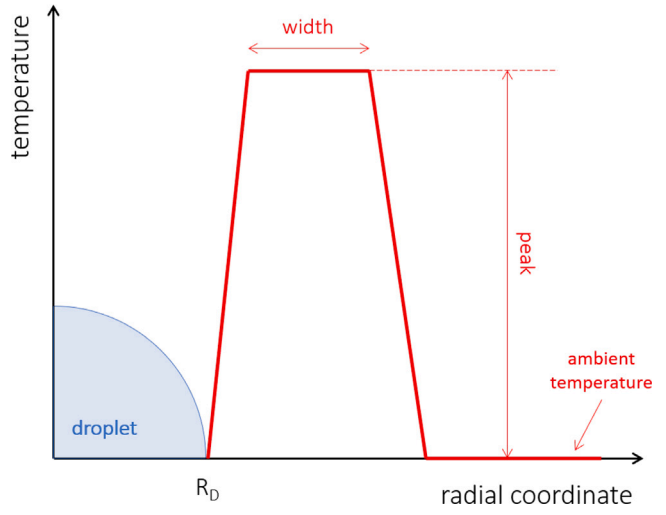

Fig. 1. Initial temperature profile in the gaseous phase for hot-wire or spark ignition cases. The temperature peak is usually assumed equal to ~2200–2500 K and the width of the imposed profile equal to ~4–6 time the droplet radius R_D.

is assumed to be constant and uniform for simplicity, the continuity equation is used to directly derive the radial velocity. This means that the continuity equation is treated as an algebraic equation rather than a differential one, unlike the species and energy transport equations. The first-order upwind discretization scheme was selected for the convective term to ensure numerical stability within the fully-coupled framework used to solve the governing equations. This approach was chosen due to the complex multi-scale nature of the problem, where steep gradients in temperature and species concentration often occur near the droplet surface. Higher-order schemes, while potentially more accurate, could introduce numerical oscillations and instability, particularly in the presence of such sharp gradients. The first-order upwind scheme offers a robust and reliable solution by minimizing these risks, thereby ensuring the convergence and stability of the solver across a wide range of conditions.

After spatial discretization, the original problem is transformed into a DAE (Differential–Algebraic Equations) system, i.e. a set of differential equations in time (Eqs. (1), (3), (4), (6) and (7)) and algebraic equations corresponding to the discretized continuity equation (Eq. (5)), the boundary conditions (Eqs. (13) to (18)), and the liquid/gas interface conditions (Eqs. (8) to (11)) (see Fig. 2).

Since the droplet first enlarges when heated and then shrinks during vaporization, a moving spatial grid was introduced to describe the moving boundaries between the droplet and the surrounding gas. In order to ensure a sufficiently fine grid close to the liquid/gas interface, where the critical gradients are located, grid stretching was applied in that region. The stretching factor and the number of points in the gaseous phase are chosen in order to have a good compromise between the accuracy close to the droplet surface and the overall size of the gaseous computational domain (whose outer radius is usually ~100 larger than the droplet's radius). In typical problems, ~50 points are adopted in the liquid phase and ~300 points in the gaseous phase.

In case detailed kinetic mechanisms are adopted, the resulting total number of DAE equations rapidly increases. For a multicomponent droplet with NL species, NG gaseous species, a computational mesh with n_L and n_G points for the liquid and gaseous phases, respectively, the total number n_E of DAE equations is: $n_E = n_L(NL+3)+5+n_G(NG+3)$. As an example, if we imagine a droplet of 4 liquid species and a detailed kinetic mechanism with ~400 species, 50 points in the liquid phase and 300 points in the gaseous phase, the total number of DAE equations would be equal to ~121,000. Such a big system of

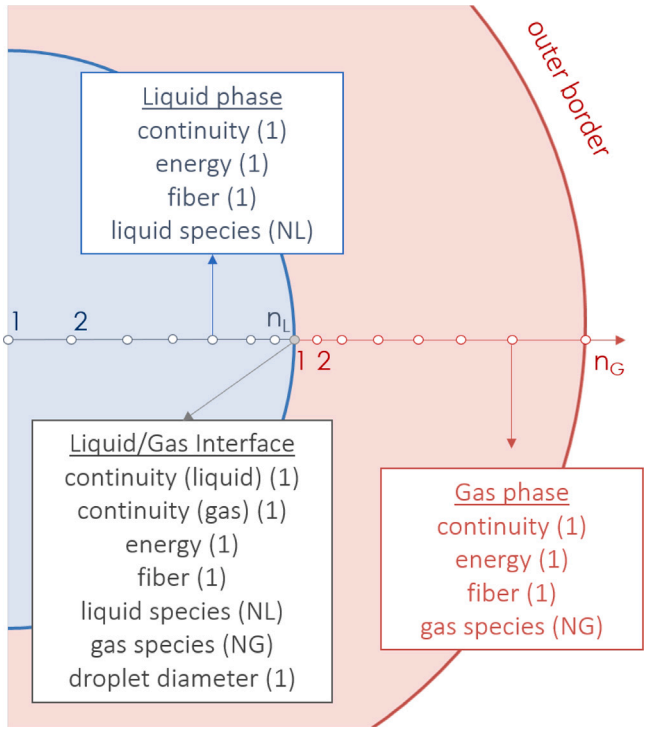

Fig. 2. Sketch of computational domain and computational grids adopted in the simulations.

differential and algebraic equations poses several numerical challenges, mainly because of:

- high non-linearity of transport equations of energy and species, mainly because of the chemical source terms (unless pure evaporation cases are considered), governed by the Arrhenius' law;
- high stiffness, due to the existence of a wide range of characteristic chemical times;
- high coupling between the conservation equations of species, because of the chemical complexity of detailed kinetic mechanisms, in which each species can be involved in a large number of reactions.

The features reported above suggests the adoption of a fully-coupled algorithm for solving the resulting DAE system. This means that all the n_E equations are advanced in time by means of a proper DAE solver for stiff problems based on implicit methods. In order to keep the computational times reasonably small, it is important to take advantage of the structured, sparse pattern of the Jacobian matrix $\mathbf{J}$ associated to the DAE system. Indeed, if the DAE equations are properly organized, the resulting Jacobian pattern is tridiagonal-block. Each block has a size equal to $n_b = NL+NG+5$.

Radiative heat transfer equations are not included directly in the DAE system described above, but the $\nabla \dot{q}_R$ term is updated only at the end of each time step of the DAE system.

3.1. The DAE solver

Let us write the DAE system by splitting the vector of unknowns $\mathbf{y}$ in two groups, differential $\mathbf{y}_1$ and algebraic $\mathbf{y}_2$:

$$\begin{cases} \frac{d\mathbf{y}_1}{dt} = \mathbf{f}_1\left(\mathbf{y}_1, \mathbf{y}_2; t\right) \\ \mathbf{f}_2\left(\mathbf{y}_1, \mathbf{y}_2; t\right) = 0 \end{cases} \tag{41}$$

where $\mathbf{f}_1$ is the r.h.s. of differential equations and $\mathbf{f}_2$ is the vector of algebraic equations. The DAE system above is solved by a specifically

conceived DAE solver for stiff problems, which exploits the block-tridiagonal structure of the associated Jacobian matrix. The DAE solver is based on the BDF technique [52] and it is derived from the BzzDae solver [53,54], from which it inherited the following features:

- if the model variables are physically bounded, the user may assign maximum and/or minimum constraint vectors. The solver automatically handles the constraints, taking care not to violate the assigned bounds. The control is performed before passing any illegal values to the DAE system routine. The correction vector, **b**, is accepted only when the nonlinear system resulting from the DAE problem is accurately solved to the assigned precision and when the unknown vector **y** simultaneously complies with the constraints. As a result, the DAE function is always computed with safe $\mathbf{y_1}$ and $\mathbf{y_2}$ values and math errors are avoided *a priori*;
- the algebraic portion of the Jacobian matrix is properly normalized [55], in order to have a **G** matrix as:

$$\mathbf{G} = \begin{bmatrix} \mathbf{I} - hr_0 \frac{\partial \mathbf{f}_1}{\partial \mathbf{y}_1} & hr_0 \frac{\partial \mathbf{f}_1}{\partial \mathbf{y}_2} \\ \frac{\partial \mathbf{f}_2}{\partial \mathbf{y}_1} & \frac{\partial \mathbf{f}_2}{\partial \mathbf{y}_2} \end{bmatrix} \tag{42}$$

  where h is the step-size and r_0 the first coefficient of the BDF method [52]. Robustness and precision of the solver are greatly improved after the normalization;
- the integration order is reduced when the elements of the Nordsieck vector are not decreasing (see [55]);
- when repeated convergence failures occur, the integration order is automatically reduced to 1 and the integration restarts from the last successful convergence step [54,56].

Droplet combustion, similarly to most combustion systems involving complex kinetic mechanisms, is characterized by a relevant number of equations and by the need to numerically evaluate the Jacobian matrix **J** several times. Since the Jacobian matrix evaluations and factorizations are very expensive operations in terms of CPU time, it is important to adopt proper strategies to reduce their number as much as possible:

- a distinct memory allocation for the Jacobian matrix and its factorization is adopted. As a consequence, when either a different step size or a method order is chosen, there is no need to re-evaluate the Jacobian matrix and then superimpose its factorization, which is required by the non-linear system solver based on the Newton method. This has obviously a big impact on the overall performances;
- with a large number of equations, the Jacobian numerical evaluation is rather time consuming, so it is advisable to delay the update of **J** as much as possible. Conversely, if the system has few equations, it is convenient to evaluate **J** more frequently in order to increase the efficiency of the Newton method. On this basis, the Jacobian matrix with a proper frequency dependent on size of **J** and CPU speed.

4. Examples

Several examples of applications of the proposed framework are reported in this section. As already mentioned, the code is able to model three different scenarios: pure evaporation, autoignition, and hot-wire (or spark) ignition of isolated droplets. Additional examples are available in recently published papers [57–60]. For further details on the sensitivity analysis regarding the mesh resolution and the boundary condition on the outer edge of the computational domain, readers are referred to the Supplementary Material accompanying this manuscript.

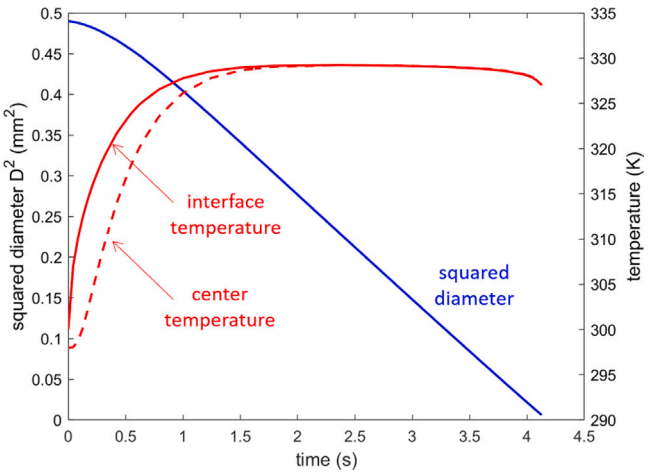

Fig. 3. Evaporation of a n-heptane droplet: initial diameter $D_0 = 0.700$ mm, pressure $P = 1$ atm, ambient temperature $T_{gas} = 500$ K.

4.1. Evaporation of single-component droplets

Pure evaporation of isolated fuel droplets in inert atmosphere (or at sufficiently low temperature so that combustion reactions cannot occur) is the simplest scenario of application of the framework. Obviously, pure evaporation means that no kinetic mechanism within the gas phase is needed, with obvious advantages on the computational side, because of the reduced number of species to be transported (fuel components and gaseous inert species only).

A representative example here considered, useful to discuss the general physics of the evaporation process, is a droplet of n-heptane (initial diameter $D_0 = 0.700$ mm and initial temperature of 298 K) evaporating in nitrogen at atmospheric pressure (P = 1 atm) and temperature T_0 = 500 K. Fig. 3 shows the temporal evolution of the squared droplet diameter (D^2 curve) and the temperatures at liquid/gas interface (T_{int}) and at the center of the droplet (T_{center}). Initially the droplet evaporates slowly: this is the initial heating phase, during which the temperature of its surface is still relatively modest. Because of such a low surface temperature, the mass fraction of n-heptane at the interface is small, resulting in a modest composition gradient in the gaseous phase (which is the driving force of the evaporation process). During this initial phase, most of the heat transferred from the gas to droplet is used for heating the droplet itself (with the consequent thermal expansion) and only a fraction is converted into latent heat of evaporation. The evaporation rate increases progressively, until it settles at a constant value (steady-state evaporation regime), evidenced by the linear dependence of D^2 on time. The temperature at the interface reaches a constant value, well below the normal boiling temperature (for n-heptane equal to 373 K). The temperature at the center of the droplet is obviously smaller than that at the interface, but the evaporation process is so slow, that the droplet temperature field becomes rapidly uniform. The slope of the D^2 curve during the steady-state evaporation phase is typically used as a measure of the vaporization rate (K_v) of the droplet. In the example considered here, we have $K_v = 0.129$ mm^2/s.

Then, we explored the vaporization of n-heptane droplets as a function of the initial droplet diameter, ambient temperature, pressure, and inert species. The results are summarized in Fig. 4.

Fig. 4a shows the D^2 curve for several initial droplet diameters (from 0.5 to 1.1 mm). Obviously, the vaporization time increases as the droplet size increases. However, it is quite easy to see that the vaporization rate is independent of the initial diameter, as suggested by the slope of the D^2 curves. This aspect would be more evident if both the axes were divided by the initial squared droplet diameter D_0^2 (not here reported). The 4 curves would almost perfectly overlap,

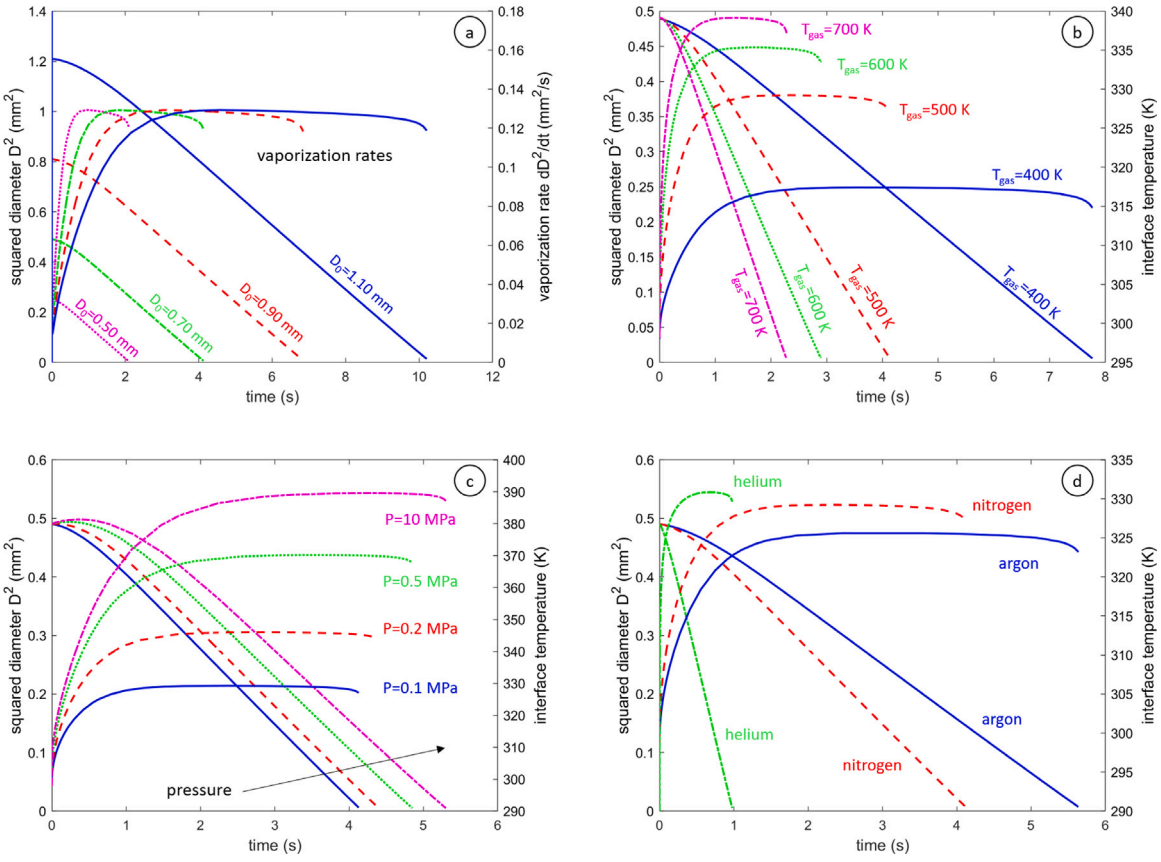

Fig. 4. Evaporation of a n-heptane droplets: sensitivity to operating conditions. (a) nitrogen, $P = 1$ atm, $T_{gas} = 500$ K; (b) nitrogen, $D_0 = 0.700$ mm, $P = 1$ atm; (c) nitrogen, $D_0 = 0.700$ mm, $T_{gas} = 500$ K; (d) $D_0 = 0.700$ mm, $P = 1$ atm; $T_{gas} = 500$ K.

becoming indistinguishable from each other (in line with experimental observations and theoretical models proposed for the evaporation of isolated droplets [61]).

Fig. 4b shows the results obtained when the ambient temperature changes. The vaporization rates are definitely different and increase, as expected, with the temperature of the environment. In particular, the vaporization speed increases from 0.066 mm^2/s at 400 K up to reaching 0.237 mm^2/s at 700 K.

Fig. 4c shows the evolution curves of D^2 as the pressure of the gaseous environment changes. The vaporization rate shows a weak dependence on pressure. Indeed, the D^2 slopes are very similar to each other, moving from 0.129 mm^2/s at 0.1 MPa to 0.120 mm^2/s at 1 MPa. However, the pressure has a strong effect on the initial heating phase, during which the droplet diameter increases because of the liquid thermal expansion. The duration of this phase increases as the pressure increases. As a result, despite the similar vaporization rates, the time required for the evaporation of the droplet is much longer at higher pressures. This effect is the direct consequence of the increase of the boiling temperature of n-heptane with pressure.

Finally, Fig. 4d shows the evolution of the droplet as a function of the inert species in the gaseous atmosphere (nitrogen, argon or helium). The vaporization rates are significantly different. As discussed by Dalili et al. [62], this can be explained by the different thermal conductivities of the three gases (0.0268 W/m/K for argon, 0.0383 W/m/K for nitrogen and 0.222 W/m/K for helium). Indeed the heat flux from the gaseous phase to the droplet is proportional to the thermal conductivity of the gaseous boundary layer surrounding the droplet, which is rich of the evaporating fuel. Thus, the very high thermal conductivity of helium results in a faster vaporization rate and in a higher liquid temperature.

Additional examples of pure vaporization are carried out considering different fuel species: n-heptane, n-decane, n-dodecane and n-hexadecane (Fig. 5). As expected, the vaporization rate decreases with increasing fuel molecular weight, because of the lower vapor pressure. The temperature at the interface during the steady-state evaporation regime is a function of the normal-boiling temperature of the fuel. The heating phase (with possible droplet expansion) shows significant differences among the n-alkanes: heavier n-alkanes have a lower vapor pressure, thus the evaporation occurs at a significant rate only when the droplet temperature is sufficiently high and this heating phase requires some time. The examples given in this paragraph show how the calculation tool can be easily adopted to explore the effect of different operating conditions (temperature, pressure, gas phase composition) on the vaporization of different pure fuels.

Before moving on to the next section, a series of comparisons between numerical simulations and experimental results are presented in order to demonstrate the accuracy of numerical predictions. In particular, we considered the measurements made by Nomura et al. [63] on isolated n-heptane droplets ($D_0 = 0.700$ mm) evaporating in inert nitrogen in a variable range of temperatures (300–800 K) and pressures (0.1 and 0.5 MPa). In the experimental tests, the droplet was suspended on a SiC fiber with a diameter of ~150 μm. Since the fiber diameter is not negligible if compared to the size of the droplet, the numerical simulations were carried out including the fiber in the set of governing equations (see Section 2.9). The comparison between experimental data and numerical simulations is summarized in Fig. 6. The simulations are able to capture the experimental data with reasonable accuracy.

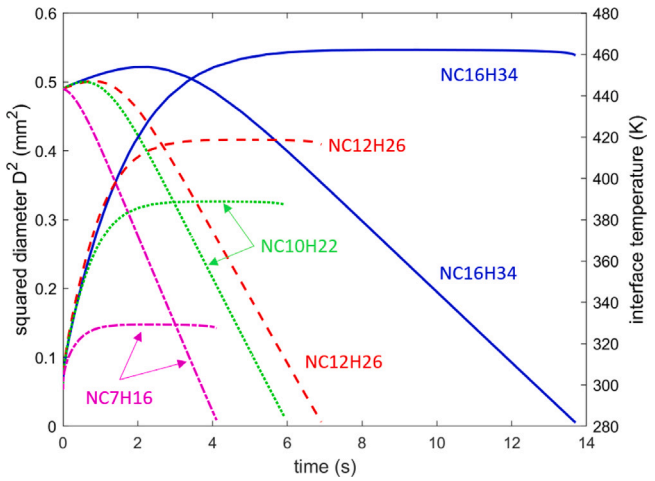

Fig. 5. Evaporation of a isolated droplets of n-heptane, n-decane, n-dodecane and n-hexadecane: initial diameter $D_0 = 0.700$ mm, pressure $P = 1$ atm, ambient temperature $T_{gas} = 500$ K.

The deviations could be partially explained by the difficulty, at the numerical level, to reproduce exactly the initial conditions experienced by the droplet during the experiments. In other words, at time $t = 0$, it is impossible to know exactly the state of the experimental system, i.e. temperature profile in the liquid and gas phases, possible presence of pre-evaporated fuel, diameter and initial shape of the drop, etc. More recently, another possible explanation, which is not necessarily mutually exclusive, has been recently proposed by Cipriano et al. [64]. They suggest that the experiments may still experience non-negligible residual gravity, thus inducing natural convection phenomena which cannot be captured by a 1D model.

4.2. Evaporation of multi-component droplets

The evaporation of a multi-component droplets represents a more complex scenario. As an example, we considered a multi-component droplet consisting of 4 n-alkanes (n-heptane, n-decane, n-dodecane, n-hexadecane), initially present in the same amount (on a mass basis). Also in this case, the droplet ($D_0 = 0.7$ mm), was assumed to evaporate in pure nitrogen at atmospheric pressure. Two different gas phase temperatures (400 K and 800 K) were considered. The vaporization times of the two droplets are significantly different, equal to 110 s and 2.7 s, respectively. Thus, for graphical reasons, the D^2 and interface temperature curves are reported in Fig. 7 as a function of a dimensionless time, obtained dividing the real time (t) by the vaporization times (t_{life}) reported above. It is clear that at high temperature (800 K) the D^2 curve has a shape similar to that already observed for single-component droplets: a (rather long) heating period is followed by a vaporization phase at a constant rate. On the contrary, at low temperature (400 K), the heating phase of the droplet is almost absent. The droplets starts evaporating quite fast, but at some point ($t/t_{vap} = 0.1 - 0.2$) the evaporation rate slows down until reaching a constant value.

The reasons for this behavior (so different from that observed for the single-component droplets) can be understood if we refer to the plots in Fig. 8, which show the average mass fractions of the 4 components inside the droplet over time. At low temperature, the components evaporate substantially in sequence, as a function of the corresponding vapor pressure. This occurs because the low temperature does not allow to reach high evaporation flows and consequently the diffusive processes inside the droplet have time enough to bring on the interface the most volatile component, which evaporates preferentially. At high temperature, the evaporation flows are much higher, so the diffusive processes become limiting. This means that the diffusion in the liquid phase is not able to feed the most volatile component to the interface, to compensate for the amount that is evaporating. As a result, all the components evaporate at the same time (although not at exactly the same rate). Thus, at low temperature we observe a sort of distillation of the droplet (*distillation limit*). At high temperature, the transport limitations inside the droplet govern its evolution (*diffusion limit*).

4.3. Hot-wire ignition of single-component droplets

The next example of application is the combustion of a droplet, ignited through a hot-wire (or a spark). As already mentioned in Section 2.11, ignition is simulated by imposing an initial non-uniform temperature radial profile close to droplet surface (in this specific example peaking at ~2400 K). A n-heptane droplet ($D_0 = 0.700$ mm) in regular air (initially at ambient temperature) was considered. The simulation was carried out using the CRECK_2003_TOT_HT detailed kinetic mechanism with 368 species and 14 462 reactions [65]. For simplicity, no low-temperature chemistry, neither soot formation were included in the mechanism. Radiative heat transfer was included via the P1 model coupled to the Weighted-Sum-of-Gray-Gases Model (WSGGM) for accounting for non-gray media effects. Ideal thermodynamic equilibrium at the interface was assumed and the ideal gas law was considered to describe the gaseous phase.

Fig. 9a reports the temporal evolution of the temperature field in the gas phase surrounding the droplet. For graphical reasons, both the spatial and temporal coordinates are reported in logarithmic scales. At sufficiently low times (<0.1 ms), the radial temperature profile is still affected by the imposed initial condition adopted for simulating the external ignition (see Fig. 1). At t =~0.1 ms the droplet ignition occurs, as evident from the short and small increase of temperature. A diffusion flame develops, fed by the evaporation of n-heptane. As evident from the 3D plot, the flame width increases during the time, reaching also the regions closer to the outer border of the computational domain. More quantitative data about the flame evolution are available in Fig. 13b, which shows the temporal evolution (linear scale) of peak temperature and flame diameter. During the steady-state evaporation regime, the flame temperature reaches a constant value of ~1950 K. The flame diameter, defined as the radial position of temperature peak (continuous line) or the radial position of OH mass fraction peak (dashed line), initially increases (up to reaching ~6 mm), then decreases.

Fig. 10 reports the calculated D^2 curve and temporal evolution of temperature at center of the droplet and at the liquid/gas interface. The D^2 curve is very similar to what already observed and discussed for pure evaporation cases: after a short initial period, during which the droplet is heated up, the vaporization reaches a steady-state regime, during which the vaporization rate remains constant. Fig. 10 also shows how the interface temperature rapidly increases, because of the flame surrounding the droplet, up to a constant value, slightly below the normal boiling temperature of n-heptane (373 K). The temperature at the center of the droplet increases slower, because the vaporization process is faster than the transfer of heat from the interface to the center of the droplet. As a consequence, a significant temperature gradient can survive inside the droplet. Only when the droplet size becomes sufficiently small (in this case at ~0.55 s), the temperature field becomes uniform.

Radial profiles of temperature and mole fractions of relevant species in the gaseous phase at t = 500 ms are available in Fig. 11. A typical diffusive burning regime is evident. O_2 becomes zero where the maximum temperature is reached. The mole fraction n-heptane at the interface is dictated by vapor–liquid equilibrium and rapidly decreases to zero in the pyrolytic region, well before the maximum temperature. The main products are H_2O, CO_2 and CO. Ethylene (C_2H_4) and acetylene (C_2H_2) are important intermediates, together with methane, benzene, and naphthalene (not here reported). As already observed in Fig. 13b, the peak position of temperature and OH radical are not exactly the same, being the OH peak located at a larger distance from the droplet surface.

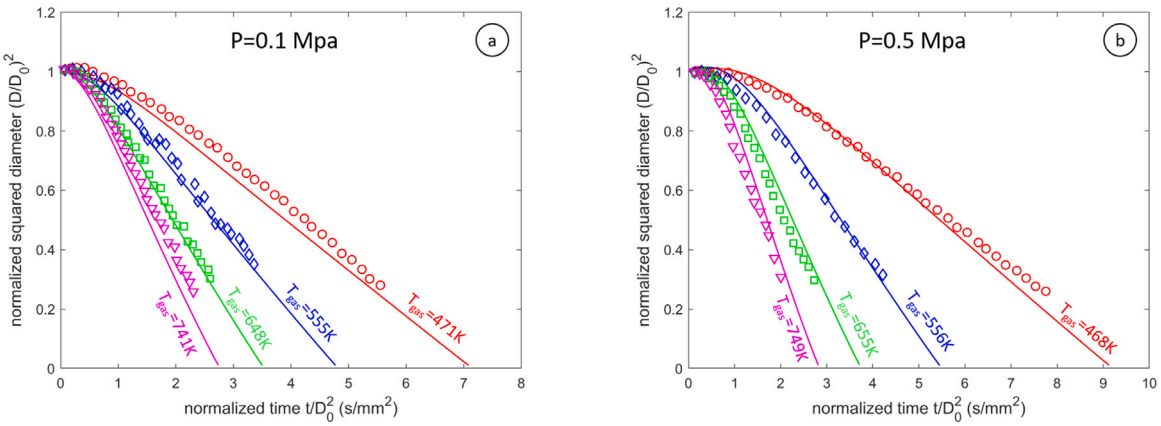

Fig. 6. Evaporation of n-heptane droplets (initial diameter $D_0 = 0.700$ mm) in nitrogen: comparison with experimental data by Nomura et al. [63] at 0.1 MPa (a) and 0.5 MPa (b).

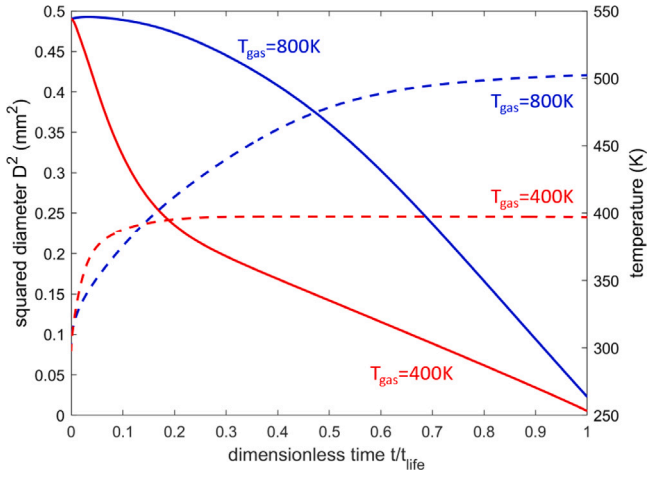

Fig. 7. Evaporation of a multicomponent droplet in nitrogen at $P = 1$ atm and temperature of 800 K (a) and 400 K (b). Initial diameter $D_0 = 0.700$ mm. Initial composition (mass fractions): 25% n-heptane, 25% n-decane, 25% n-dodecane, 25% n-hexadecane.

Similarly to what we did in Section 4.1, we explored the ignition of n-heptane droplets as a function of the initial droplet diameter and ambient pressure. The results are summarized in Fig. 12. As expected, in agreement with theoretical models developed for combustion of isolated droplets in quiescent environments [61], the vaporization rate is basically independent of the initial droplet diameter (Fig. 12a). The pressure of the gaseous phase has a more complex impact on the evolution of the droplet (Fig. 12b). The vaporization rate slightly increases for increasing pressure, while the flame diameter decreases and its peak value is reached at larger times.

As a final example, additional simulations were carried out considering different fuels: n-heptane, n-decane and ethanol (Fig. 13). N-heptane and n-decane droplets have very similar features, in terms of both vaporization rate and flame diameters. The main difference is related to the initial heating-up phase, which is longer for the n-decane droplet, justified by its lower vapor pressure. The ethanol droplet behavior shows some significant differences: if compared to n-heptane and n-decane, its vaporization rate is much smaller and the flame is located much closer to the droplet surface. This result seems to be counter-intuitive, since ethanol has the lowest boiling temperature (~351 K), thus a larger vaporization rate would be expected. However, some points are to be considered: (i) the ethanol flame temperature (not here reported) is ~120 K colder than n-heptane and n-decane; (ii) the ethanol vaporization heat (in mass units) is more than 2 times larger than n-heptane and n-decane; (iii) re-absorption of water from the gaseous phase (not here reported) was predicted by the simulation, which slows down the whole vaporization process. The combination of these 3 factors can easily explain the results reported in Fig. 5.

4.4. Hot-wire ignition of n-heptane droplets in helium/oxygen atmosphere

Nayagam et al. [1] reported experiments on free-floated n-heptane droplet combustion carried out at 1 atm in different oxygen–helium environments on-board the STS–83 flight of the Space Shuttle Columbia during the first Microgravity Science Laboratory mission (MSL-1). The ignition was carried out using two diametrically opposed hot-wired igniters. Here we focus on experiments in atmospheres containing 35% of helium. Three initial diameters were considered, equal to 1.90, 3.10 and 4.100 mm. The simulations were carried out using the CRECK_2003_TOT_HT_LT detailed kinetic mechanism, accounting for both low- and high-temperature chemistry (492 species and 17790 reactions) [65]. No soot formation was accounted for in the simulations. Radiative heat transfer was included via the P1 model coupled to the Weighted-Sum-of-Gray-Gases Model (WSGGM) for accounting for non-gray media effects. Ideal thermodynamic equilibrium at the interface was assumed and the ideal gas law was considered to describe the gaseous phase.

Fig. 14 compares the numerical simulations with the experimental data in terms of droplet squared diameter and flame diameter. The agreement between numerical results and experimental measurements is particularly good for 1.90 and 3.10 mm droplets, especially for D^2 curves. Deviations are more evident for the flame diameter, which is always numerically over-estimated with respect to experiments. We suspect the disagreement can be explained on the basis of different definitions of flame diameter: numerically it is defined as the radial location of maximum temperature, while experimentally it is evaluated as the radial location of maximum flame-image intensity. Since formation of soot was experimentally evident, probably the zone of maximum flame intensity is located in the soot-rich region, which is typically located between the droplet surface and the flame front (see Section 4.6 for more details). This would explain why, despite the vaporization rate is correctly captured by the model, the experimental flame diameter is always smaller than the numerical one.

The case with a 4.10 mm droplet is more complex. The experimentally measured D^2 curve clearly shows the presence of two different combustion regimes. During the first phase (from time t = 0 to approximately t = 2.2 s) the droplet reaches a steady-state regime characterized by a high vaporization rate ($K_v = 1.18$ mm^2/s). Then, at ~2.2 s the vaporization rate starts decreasing, reaching a new constant, lower value ($K_v = 0.89$ mm^2/s). This *anomalous* behavior is confirmed by the numerical simulations, which reveal something interesting. In particular, if we look at the peak temperature in the gaseous phase (see Fig. 15), we observe a complex evolution for the 4.10 mm case.

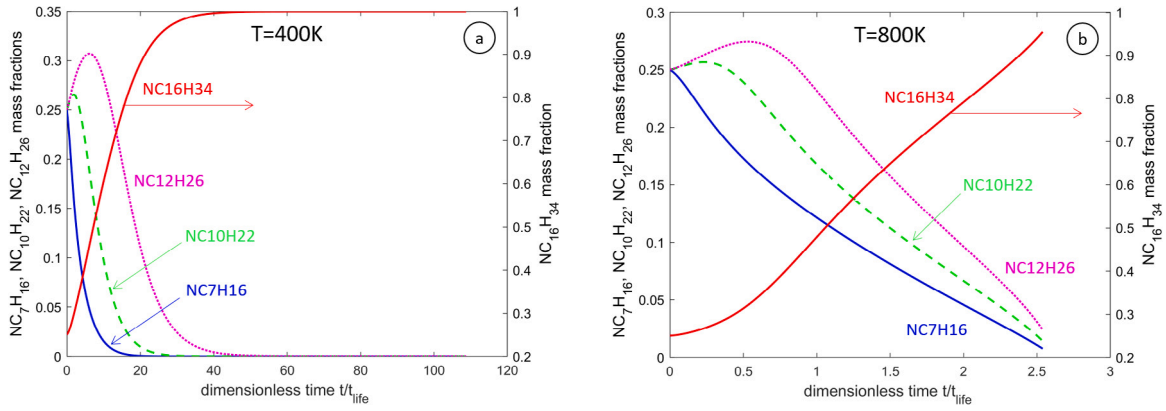

Fig. 8. Temporal evolution of mass fractions of liquid components of a multicomponent droplet evaporating in nitrogen at $P = 1$ atm and temperature of 800 K (a) and 400 K (b). Initial diameter $D_0 = 0.700$ mm. Initial composition (mass fractions): 25% n-heptane, 25% n-decane, 25% n-dodecane, 25% n-hexadecane.

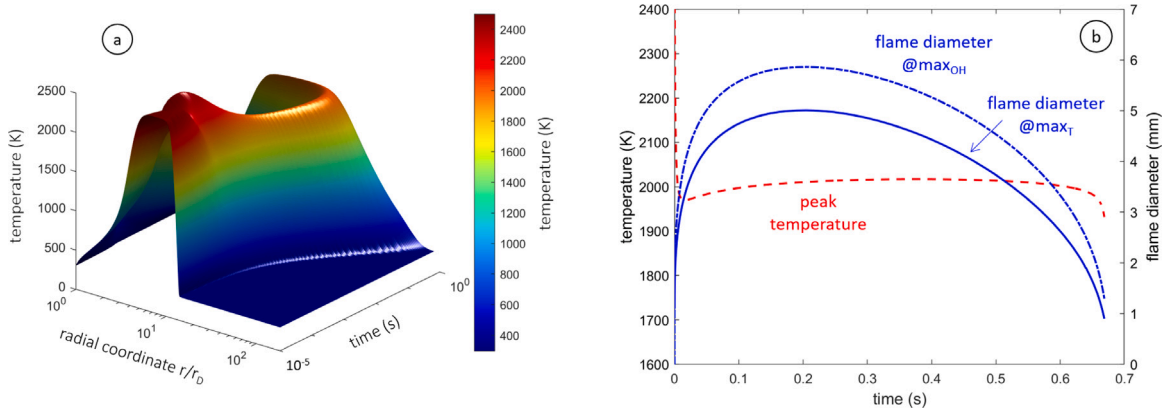

Fig. 9. Hot-wire ignition of a n-heptane droplet in air at atmospheric pressure (D_0 = 0.700 mm). (a) Temporal evolution of radial temperature profile; (b) temporal profiles of peak temperature and flame diameter.

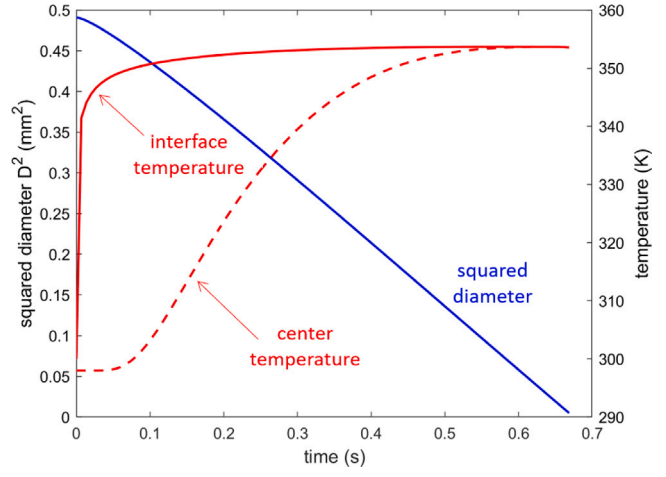

Fig. 10. Hot-wire ignition of a n-heptane droplet in air at atmospheric pressure (D_0 = 0.700 mm). Temporal evolution of squared diameter and temperatures at the center of the droplet and at the liquid/gas interface.

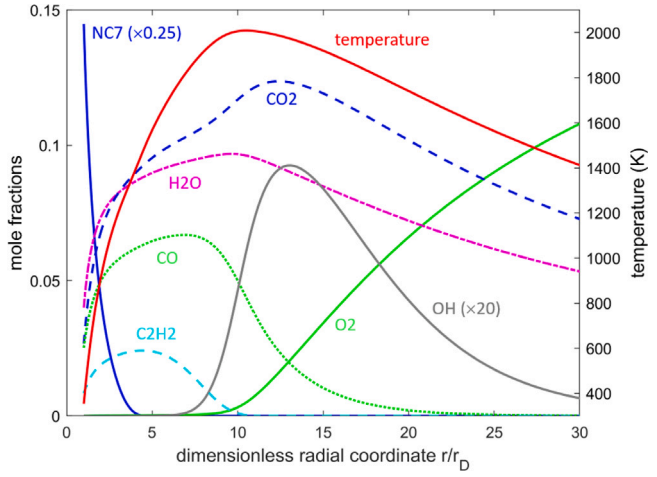

Fig. 11. Hot-wire ignition of a n-heptane droplet in air at atmospheric pressure (D_0 = 0.700 mm): radial profiles of temperature (right axis) and mole fractions of selected species at t = 500 ms.

Indeed, according to the simulations, the transition from the first to the second regime corresponds to a partial extinction of the diffusion flame, followed by the formation of a stable low-temperature flame at ~700 K, which persists around the droplet for a long period of time. Then, a second extinction occurs. Such a complex behavior can be captured only by considering the low-temperature chemistry of n-heptane in the numerical simulations. If we adopted high-temperature chemistry only, the numerical results would be in complete disagreement with the experimental data, as shown by the dashed line in Fig. 14a. Accurately predicting flame extinction is a critical test of the model's robustness and reliability, as it directly reflects the code's ability to capture complex combustion dynamics.

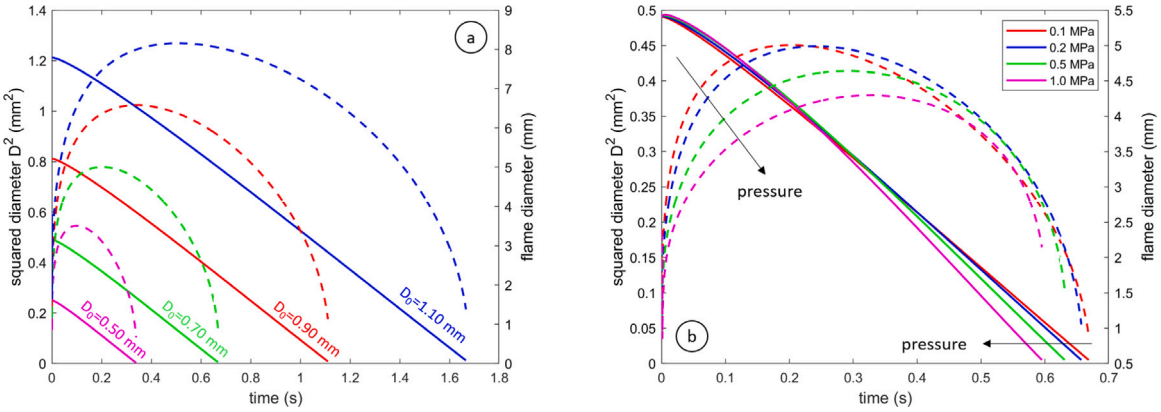

Fig. 12. Hot-wire ignition of n-heptane droplets in regular air. (a) Sensitivity to the initial diameter at $P = 1$ atm; (b) sensitivity to environment pressure for $D_0 = 0.700$ mm. The continuous lines are the squared diameter and the dotted lines are the flame diameter.

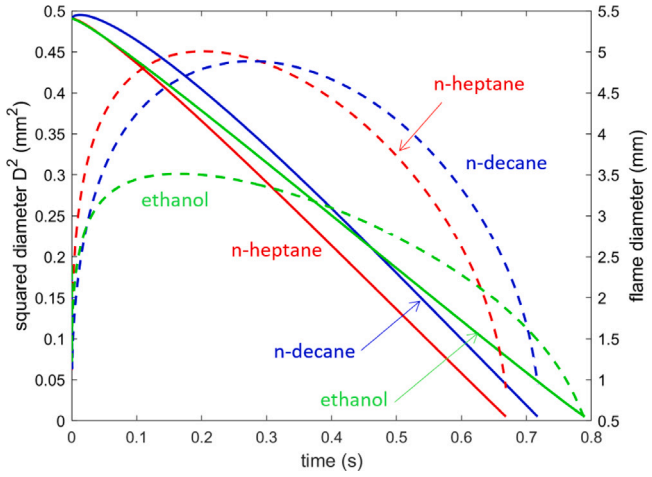

Fig. 13. Hot-wire ignition of a n-heptane droplet in air at atmospheric pressure (D_0 = 0.700 mm): radial profiles of temperature (right axis) and mole fractions of selected species at t = 500 ms. The continuous lines are the squared diameter and the dotted lines are the flame diameter.

4.5. Autoignition of n-decane droplets

The following example refers to the autoignition of n-decane droplets. This is an additional demonstration of the relevance of numerical simulations of isolated fuel droplet for better interpreting experimental data. Xu et al. [66] carried out experiments on evaporation and autoignition of isolated fuel droplets of pure n-decane in regular air (atmospheric pressure) at different temperatures, from 633 K to 1123 K. Here we focus the attention on the experiments carried out at 633 K, in which 3 different initial diameters (0.91, 1.22 and 1.56 mm) were considered. These cases were classified by Xu et al. [66] as pure evaporation cases, since no visible flame was experimentally observed. However, numerical simulations revealed a different scenario. Fig. 16a reports the D^2 curves calculated numerically without considering chemical reactions in the gaseous phase, i.e. as pure evaporation conditions. During the initial heating-up period (~1 s), the expansion of the droplet prevails over the evaporation phase. Then, a linear evolution of the squared diameter is observed, as expected for usual evaporation cases. However, the deviation of numerical results (dashed lines) from the experimental data is significant: in particular, the calculated vaporization rate is at least a factor of ~2 smaller than the experimental value. If the numerical simulations are repeated including the low-temperature chemistry for n-decane in the gaseous phase, the evolution of the droplets changes significantly (continuous lines) and the agreement with the experimental data becomes very good. This is a clear evidence of the formation of cool flames. Fig. 16b reports the peak temperature in the gaseous phase when the low-temperature chemistry is included in the simulation. All the profiles show dumped cool flames, followed by a stable temperature plateau. The dumped cool flames result from the combination of the progressive consumption of fuel and gas-phase heating. Once the first flame ignites, fuel is consumed and only partially replaced by the relatively slow vaporization. This prevents a second, high-temperature ignition. The cool flames occur at increasing frequency, produce less heat, and gradually move the system to a steady-state combustion regime. The plateau temperatures of the cool flames increase with increasing initial diameter, from ~740 K for the 0.91 mm droplet to ~760 K for the 1.57 mm droplet. This explains the slightly higher vaporization rate of the larger droplet (numerically and experimentally observed). During the dumped cool flame regime, the radial position of the peak temperature (not here reported) is very close to the droplet surface (~1.5–2.5 mm), while during the second phase (characterized by the plateau temperature) it slowly decreases with time.

Fig. 17 shows the calculated radial profiles of temperature and main species at t = 3 s for the 1.22 mm droplet. We can clearly recognize the typical structure of a low-temperature flame. Because of the lower reactivity of the system, fuel and oxygen are able to co-exist in the region close to the droplet surface and their concentration profiles are smoother than in a hot-temperature flame. Moreover, a significant mass fraction of ketohydroperoxide (NC10H22–OQOOH) is evident close to the droplet surface, confirming the active role of low-temperature mechanisms.

4.6. Hot-wire ignition of a multi-component droplet

The last example is the hot-wire ignited combustion of a multi-component droplet, experimentally studied by Cuoci et al. [67], burning in regular air at atmospheric pressure. The fuel is a 7-component mixture (termed S3) comprised of (volume fraction) n-heptane (0.11), n-pentane (0.088), iso-octane (0.405), cyclo-pentane (0.055), toluene (0.18), 1-hexene (0.063) and ethanol (0.099). The initial diameter of the droplet was equal to 0.636 mm. A detailed kinetic mechanism was adopted, including a soot model based on the discrete sectional method, able to account for nucleation, surface growth, oxidation, and

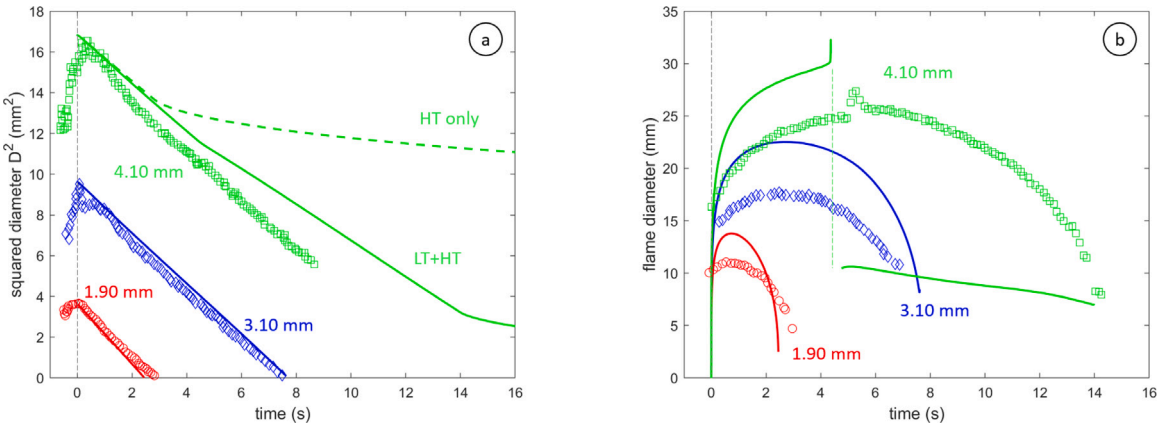

Fig. 14. Hot-wire ignition of n-heptane droplets in oxygen/helium (35/65, molar basis) atmosphere at atmospheric pressure: comparison between numerical simulations (lines) and experimental measurements.
Source: From [1].

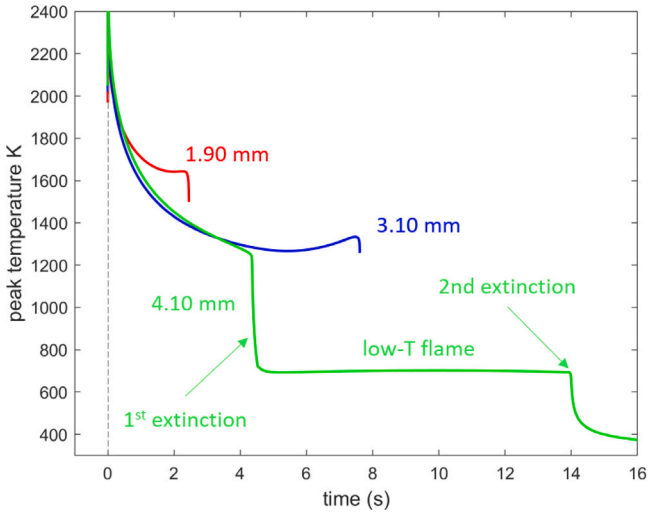

Fig. 15. Hot-wire ignition of n-heptane droplets in oxygen/helium (35/65, molar basis) atmosphere at atmospheric pressure: temporal evolution of peak temperature in the gaseous phase.

coalescence/aggregation of soot particles [68]. The total number of species and reactions is equal to 398 and 24,814, respectively. No low-temperature chemistry was included in the mechanism. The simulation is very challenging from the numerical point of view, because of the large number of species, the presence of soot particles (having a significant role in the radiative heat transfer), and the multi-component nature of the droplet, including species with a wide range of vapor pressures.

Fig. 18a shows the predicted squared droplet diameter, compared with the experimental measurements. The predictions agree well with the measurements when the soot model is included in the simulation (continuous line). Without the soot model, droplets burn significantly faster because more heat is transferred to the droplets. Indeed, soot formation significantly reduces the flame temperature because of the strong radiative losses and the endothermic reactions associated to the formation of soot itself.

Fig. 18b reports a comparison between the experimentally measured and the calculated flame stand-off ratio (FSR), i.e. the ratio between the flame diameter (defined as the position of temperature peak or the position of OH mass fraction peak) and the current droplet diameter. Also in this case, the agreement is quite satisfactory: in particular, the peak gas temperature represents well the relative position of the flame to the droplet early in the burning process, while later in burning the peak OH concentration better determines the flame diameter.

Predictions of the soot stand-off ratio (SSR), i.e. the ratio between the soot shell diameter and the current droplet diameter, are shown in Fig. 18b. The soot shell diameter is numerically defined as the diameter where soot volume fraction reaches its peak value. The trends are consistent with the data, but the predictions are overestimated. Given the challenges of measuring the flame and soot shell diameters (which are based on user-defined boundaries in the photographs) [67], the simulations show a reasonable accuracy and predictive capability in predicting the trends in the evolution of flame and soot shell diameters.

Fig. 19 shows the evolution of the S3 component mass fractions (averaged) inside the droplet. Toluene is the most non-volatile component, thus it is slow to evaporate and it accumulates inside the droplet. Because of the high temperature in the gaseous phase, the droplet experiences the so-called *diffusion limit* regime (see Section 4.2): the remaining components evaporate at similar rates, so their relative weights remains almost constant during the evolution of the droplet.

5. Conclusions

In this work, we described a comprehensive numerical framework for simulating the evaporation and combustion of isolated, spherically-symmetric, multi-component fuel droplets. The framework solves the transport equations of mass, species, and energy in both the liquid and gaseous phases and incorporates detailed kinetic mechanisms involving hundreds of species and thousands of reactions. It includes a detailed treatment of diffusion processes, thermodynamic equilibrium, and radiative heat transfer.

We have successfully tested the proposed framework under a wide range of conditions, including pure evaporation, autoignition, and hot-wire ignition scenarios. The code has demonstrated its capability to simulate complex scenarios, including the formation of oscillating cold flames and radiative extinctions. Comparisons with available experimental data have confirmed the tool's good predictive capabilities.

The proposed framework offers significant potential for advancing our understanding of the complex combustion processes of multi-component liquid fuels. It provides a robust tool for researchers and experimentalists to better plan and interpret experiments involving isolated fuel droplets. This tool is particularly relevant for studying the

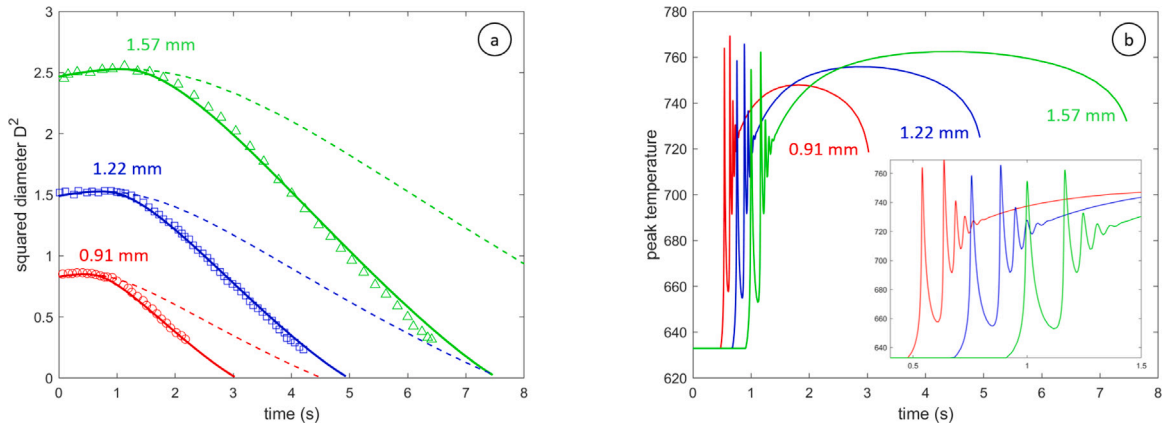

Fig. 16. Autoignition of n-decane droplets: comparison between experimental data (points) [66] and numerical calculations (lines). The continuous lines refer to the simulations carried out including the low-temperature mechanism. The dashed lines were obtained by considering the high-temperature chemistry only.

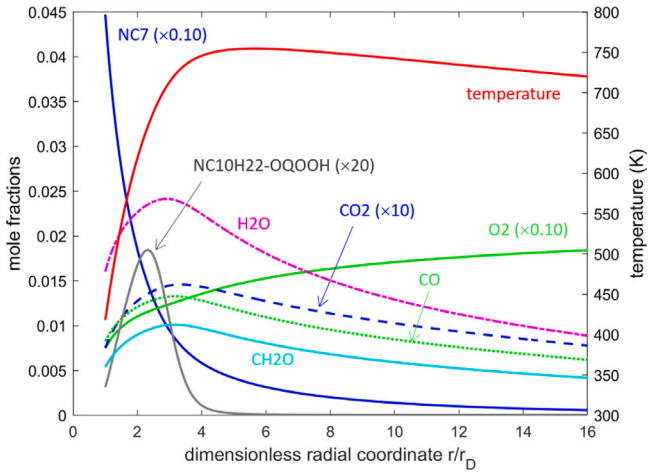

Fig. 17. Autoignition of n-decane droplets. Radial profiles of temperature (right axis) and mole fractions of selected species at t = 3 s for the 1.22 mm droplet.

fundamental aspects of droplet combustion, optimizing fuel formulations, and improving combustion efficiency in practical applications. By facilitating detailed simulations and accurate predictions, the framework can drive innovations in fuel technology and contribute to the development of cleaner and more efficient combustion systems.

Looking ahead, several promising extensions and future research directions can enhance this framework. The most notable is the extension to multidimensional configurations, enabling the study of droplet–droplet interactions, non-spherical droplet shapes, buoyancy and forced convection effects, and interactions with surfaces. This extension is already underway within our research group. Specifically, Saufi et al. [20] implemented a numerical algorithm based on the Volume-Of-Fluid (VOF) methodology in the OpenFOAM framework [69] to model the evaporation of 2D isolated droplets, showing excellent agreement with experimental data across various conditions, including high pressures. More recently, Cipriano et al. [70,71] proposed and implemented an innovative multidimensional model for multicomponent evaporation in interface-resolved simulations using a geometric VOF approach in the Basilisk sandbox [72]. Future steps will include the incorporation of chemical reactivity in the gaseous phase and a more advanced treatment of the thermodynamic properties of the liquid phase mixture.

The current framework is designed for subcritical conditions, where liquid and gas phases are distinctly separated and conventional thermodynamic models are valid. However, under supercritical conditions, where fluid properties change significantly and phase boundaries blur, the model may not fully capture the dynamics of evaporation and combustion. Future work will focus on extending the model to incorporate equations of state and transport models suitable for supercritical fluids, enhancing its applicability. Until then, users should be aware of these limitations when applying the model to scenarios involving pressures and temperatures above the critical point.

In summary, the framework presented in this work is a powerful tool for the detailed simulation of droplet combustion, offering a wide range of applications and significant potential for future development and research.

CRediT authorship contribution statement

Alberto Cuoci: Writing – review & editing, Writing – original draft, Validation, Software, Methodology, Investigation, Formal analysis, Conceptualization. **Edoardo Cipriano:** Writing – review & editing, Validation, Software, Methodology. **Abd Essamade Saufi:** Writing – review & editing, Software, Methodology. **Alessio Frassoldati:** Writing – review & editing, Methodology.

Declaration of competing interest

The authors declare that they have no known competing financial interests or personal relationships that could have appeared to influence the work reported in this paper.

Data availability

The framework described in this work is part of the `OpenSMOKE++ Suite` [21], a comprehensive collection of numerical tools for the simulation of combustion and reactive systems. The `OpenSMOKE++ Suite` is available for download at https://www.opensmokepp.polimi.it upon user registration.

Appendix A. Supplementary data

Supplementary material related to this article can be found online at https://doi.org/10.1016/j.jocs.2024.102453.

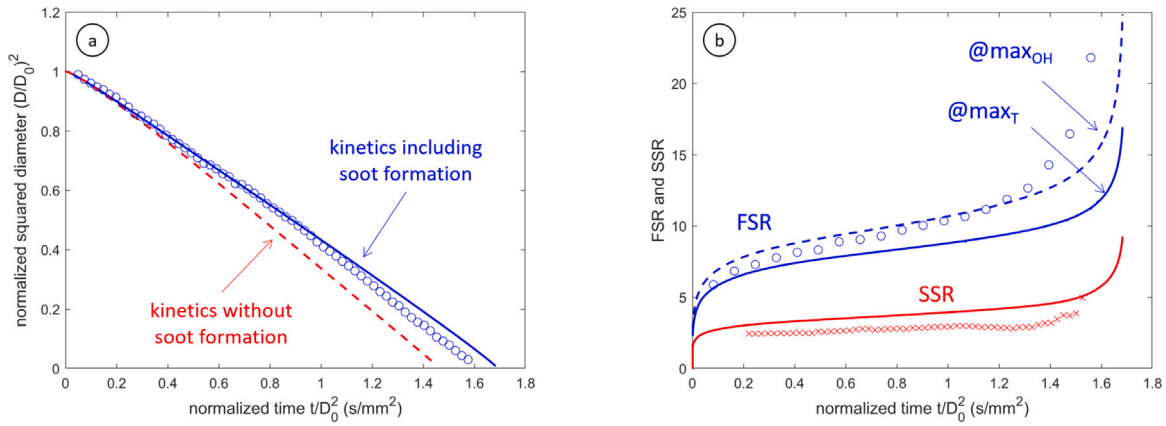

Fig. 18. Hot-wire ignited combustion of S3 droplets (D_0 = 0.636 mm): comparison between experimental measurements (points) [67] and numerical results. (a) Squared droplet diameter; (b) flame stand-off ratio (FSR) and soot stand-off ratio (SSR).

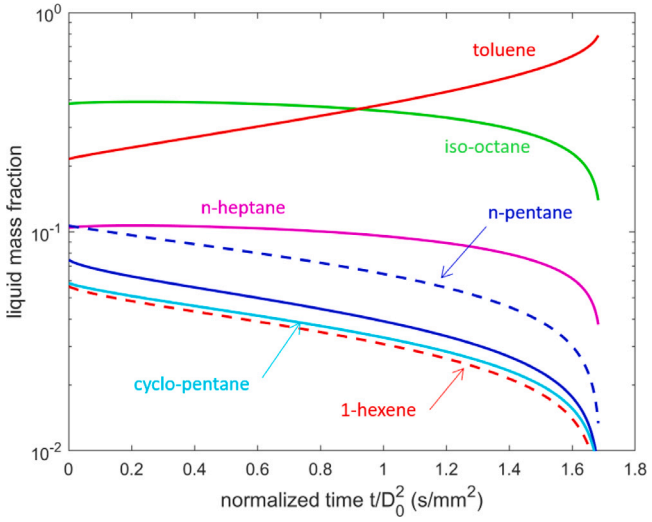

Fig. 19. Hot-wire ignited combustion of S3 droplets (D_0 = 0.636 mm): temporal evolution of average mass fractions of liquid components inside the droplet.

References

[1] V. Nayagam, J. Haggard Jr., R. Colantonio, A. Marchese, F. Dryer, B. Zhang, F. Williams, Microgravity n-heptane droplet combustion in oxygen-helium mixtures at atmospheric pressure, AIAA J. 36 (8) (1998) 1369–1378, http://dx.doi.org/10.2514/2.557.

[2] A. Marchese, F. Dryer, V. Nayagam, Numerical modeling of isolated n-alkane droplet flames: Initial comparisons with ground and space-based microgravity experiments, Combust. Flame 116 (3) (1999) 432–459, http://dx.doi.org/10.1016/S0010-2180(98)00109-6.

[3] A. Stagni, L. Esclapez, P. Govindaraju, A. Cuoci, T. Faravelli, M. Ihme, The role of preferential evaporation on the ignition of multicomponent fuels in a homogeneous spray/air mixture, Proc. Combust. Inst. 36 (2) (2017) 2483–2491, http://dx.doi.org/10.1016/j.proci.2016.06.052.

[4] C. Law, Recent advances in droplet vaporization and combustion, Prog. Energy Combust. Sci. 8 (3) (1982) 171–201, http://dx.doi.org/10.1016/0360-1285(82)90011-9.

[5] C. Avedisian, Recent advances in soot formation from spherical droplet flames at atmospheric pressure, J. Propuls. Power 16 (4) (2000) 628–635, http://dx.doi.org/10.2514/2.5619.

[6] A. Marchese, F. Dryer, The effect of liquid mass transport on the combustion and extinction of bicomponent droplets of methanol and water, Combust. Flame 105 (1–2) (1996) 104–122, http://dx.doi.org/10.1016/0010-2180(95)00179-4.

[7] A. Kazakov, J. Conley, F. Dryer, Detailed modeling of an isolated, ethanol droplet combustion under microgravity conditions, Combust. Flame 134 (4) (2003) 301–314, http://dx.doi.org/10.1016/S0010-2180(03)00091-9.

[8] D. Dietrich, V. Nayagam, M. Hicks, P. Ferkul, F. Dryer, T. Farouk, B. Shaw, H. Suh, M. Choi, Y. Liu, C. Avedisian, F. Williams, Droplet combustion experiments aboard the international space station, Microgravity Sci. Technol. 26 (2) (2014) 65–76, http://dx.doi.org/10.1007/s12217-014-9372-2.

[9] A. Hall, J. Diederichsen, An experimental study of the burning of single drops of fuel in air at pressures up to twenty atmospheres, Symp. (Int.) Combust. 4 (1) (1953) 837–846, http://dx.doi.org/10.1016/S0082-0784(53)80109-8.

[10] M. Goldsmith, Experiments on the burning of single drops of fuel, J. Jet Propul. 26 (1956).

[11] D. Dietrich, J. Haggard Jr., F. Dryer, V. Nayagam, B. Shaw, F. Williams, Droplet combustion experiments in spacelab, Symp. (Int.) Combust. 26 (1) (1996) 1201–1207, http://dx.doi.org/10.1016/S0082-0784(96)80336-5.

[12] V. Nayagam, D. Dietrich, M. Hicks, F. Williams, Cool-flame extinction during n-alkane droplet combustion in microgravity, Combust. Flame 162 (5) (2015) 2140–2147, http://dx.doi.org/10.1016/j.combustflame.2015.01.012.

[13] T.I. Farouk, F.L. Dryer, Extinction characteristics of isolated n-alkane fuel droplets during low temperature cool flame burning in air, Proc. Combust. Inst. 39 (2) (2023) 2471–2481, http://dx.doi.org/10.1016/j.proci.2022.07.094.

[14] T. Farouk, F. Dryer, On the extinction characteristics of alcohol droplet combustion under microgravity conditions - A numerical study, Combust. Flame 159 (10) (2012) 3208–3223, http://dx.doi.org/10.1016/j.combustflame.2012.04.005.

[15] M. Choi, L. Kyeong-Okk, Investigation of sooting in microgravity droplet combustion, Symp. (Int.) Combust. 26 (1) (1996) 1243–1249, http://dx.doi.org/10.1016/S0082-0784(96)80341-9.

[16] K.-O. Lee, S.L. Manzello, M.Y. Choi, The effects of initial diameter on sooting and burning behavior of isolated droplets under microgravity conditions, Combust. Sci. Technol. 132 (1–6) (1998) 139–156, http://dx.doi.org/10.1080/00102209808952013.

[17] S. Manzello, M. Choi, A. Kazakov, F. Dryer, R. Dobashi, T. Hirano, The burning of large n-heptane droplets in microgravity, Proc. Combust. Inst. 28 (1) (2000) 1079–1086, http://dx.doi.org/10.1016/S0082-0784(00)80317-3.

[18] A. Stagni, A. Cuoci, A. Frassoldati, E. Ranzi, T. Faravelli, Numerical investigation of soot formation from microgravity droplet combustion using heterogeneous chemistry, Combust. Flame 189 (2018) 393–406, http://dx.doi.org/10.1016/j.combustflame.2017.10.029.

[19] V. Nayagam, D. Dietrich, P. Ferkul, M. Hicks, F. Williams, Can cool flames support quasi-steady alkane droplet burning?, Combust. Flame 159 (12) (2012) 3583–3588, http://dx.doi.org/10.1016/j.combustflame.2012.07.012.

[20] A.E. Saufi, A. Frassoldati, T. Faravelli, A. Cuoci, DropletSMOKE++: a comprehensive multiphase CFD framework for the evaporation of multidimensional fuel droplets Int. J. Heat Mass Transfer 131 (2019) 836–853.

[21] A. Cuoci, A. Frassoldati, T. Faravelli, E. Ranzi, OpenSMOKE++: An object-oriented framework for the numerical modeling of reactive systems with detailed kinetic mechanisms Comput. Phys. Comm. 192 (2015) 237–264.

[22] T. Farouk, F. Dryer, Microgravity droplet combustion: Effect of tethering fiber on burning rate and flame structure Combust. Theory Model. 15 (4) (2011) 487–515, http://dx.doi.org/10.1080/13647830.2010.547601.

[23] C.L. Yaws, The Yaws Handbook of Physical Properties for Hydrocarbons and Chemicals, Gulf Professional Publishing, 2015.

[24] P. Keller, A. Bader, C. Hasse, The influence of intra-droplet heat and mass transfer limitations in evaporation of binary hydrocarbon mixtures Int. J. Heat Mass Transfer 67 (2013) 1191–1207.

[25] A. Perea, P. Garcia-Ybarra, J. Castillo, Soot diffusive transport effects affecting soot shell formation in droplet combustion in: Mediterranean Combustion Symposium, 1999, pp. 275–285.

[26] G. Ben-Dor, T. Elperin, B. Krasovit, Effect of thermo–and diffusiophoretic forces on the motion of flame-generated particles in the neighbourhood of burning droplets in microgravity conditions in: Proceedings of the Royal Society of London A: Mathematical, Physical and Engineering Sciences, Vol. 459, The Royal Society, 2003, pp. 677–703.

[27] R. Taylor, R. Krishna, Multicomponent Mass Transfer, Vol. 2, John Wiley & Sons, 1993.
[28] J. Wesselingh, R. Krishna, Mass Transfer, Ellis Horwood Chichester, West Sussex (England), 1990.
[29] M. Siddiqi, K. Lucas, Correlations for prediction of diffusion in liquids Can. J. Chem. Eng. 64 (5) (1986) 839–843.
[30] J.M. Prausnitz, R.N. Lichtenthaler, E.G. de Azevedo, Molecular Thermodynamics of Fluid-Phase Equilibria, Pearson Education, 1998.
[31] S. Chapman, T.G. Cowling, The Mathematical Theory of Non-Uniform Gases: An Account of the Kinetic Theory of Viscosity, Thermal Conduction and Diffusion in Gases, Cambridge University Press, 1970.
[32] M. Smooke, C. McEnally, L. Pfefferle, R. Hall, M. Colket, Computational and experimental study of soot formation in a coflow, laminar diffusion flame Combust. Flame 117 (1) (1999) 117–139.
[33] T.P. Coffee, J.M. Heimerl, Sensitivity analysis for premixed, laminar, steady state flames Combust. Flame 50 (1983) 323–340.
[34] G. Dixon-Lewis, Flame structure and flame reaction kinetics II. Transport phenomena in multicomponent systems Proc. R. Soc. Lond. Ser. A Math. Phys. Eng. Sci. 307 (1488) (1968) 111–135, http://dx.doi.org/10.1098/rspa.1968.0178.
[35] G. Santachiara, F. Prodi, C. Cornetti, Experimental measurements on thermophoresis in the transition region J. Aerosol Sci. 33 (5) (2002) 769–780.
[36] M.F. Modest, Radiative Heat Transfer, Academic Press, 2013.
[37] R. Viskanta, R.L. Merriam, Heat transfer by combined conduction and radiation between concentric spheres separated by radiating medium J. Heat Transfer 90 (2) (1968) 248–255, http://dx.doi.org/10.1115/1.3597493.
[38] M.F. Modest, The weighted-sum-of-gray-gases model for arbitrary solution methods in radiative transfer J. Heat Transfer 113 (3) (1991) 650–656.
[39] S.W. Baek, J.H. Park, C.E. Choi, Investigation of droplet combustion with nongray gas radiation effects Combust. Sci. Technol. 142 (1–6) (1999) 55–79.
[40] T. Smith, Z. Shen, J. Friedman, Evaluation of coefficients for the weighted sum of gray gases model J. Heat Transfer 104 (4) (1982) 602–608.
[41] C. Yin, Refined weighted sum of gray gases model for air-fuel combustion and its impacts Energy Fuels 27 (10) (2013) 6287–6294.
[42] T.F. Smith, A.M. Al-Turki, K.-H. Byun, T.K. Kim, Radiative and conductive transfer for a gas/soot mixture between diffuse parallel plates J. Thermophys. Heat Transfer 1 (1) (1987) 50–55.
[43] F. Cassol, R. Brittes, F.H. França, O.A. Ezekoye, Application of the weighted-sum-of-gray-gases model for media composed of arbitrary concentrations of H_2O, CO_2 and soot Int. J. Heat Mass Transfer 79 (2014) 796–806.
[44] D.-Y. Peng, D.B. Robinson, A new two-constant equation of state Ind. Eng. Chem. Fundam. 15 (1) (1976) 59–64, http://dx.doi.org/10.1021/i160057a011.
[45] A. Fredenslund, R.L. Jones, J.M. Prausnitz, Group-contribution estimation of activity coefficients in nonideal liquid mixtures AIChE J. 21 (6) (1975) 1086–1099, http://dx.doi.org/10.1002/aic.690210607.
[46] S.W. Churchill, H.H. Chu, Correlating equations for laminar and turbulent free convection from a horizontal cylinder Int. J. Heat Mass Transfer 18 (9) (1975) 1049–1053, http://dx.doi.org/10.1016/0017-9310(75)90222-7.
[47] G. Andrews, D. Bradley, G. Hundy, Hot wire anemometer calibration for measurements of small gas velocities Int. J. Heat Mass Transfer 15 (10) (1972) 1765–1786, http://dx.doi.org/10.1016/0017-9310(72)90053-1.
[48] D.C. Collis, M.J. Williams, Two-dimensional convection from heated wires at low Reynolds numbers J. Fluid Mech. 6 (3) (1959) 357–384, http://dx.doi.org/10.1017/S0022112059000696.
[49] S. Cho, M. Choi, F. Dryer, Extinction of a free methanol droplet in microgravity in: Symposium (International) on Combustion, Vol. 23, Elsevier, 1991, pp. 1611–1617.
[50] A. Cuoci, M. Mehl, G. Buzzi-Ferraris, T. Faravelli, D. Manca, E. Ranzi, Autoignition and burning rates of fuel droplets under microgravity Combust. Flame 143 (3) (2005) 211–226.
[51] A. Cuoci, A.E. Saufi, A. Frassoldati, D.L. Dietrich, F.A. Williams, T. Faravelli, Flame extinction and low-temperature combustion of isolated fuel droplets of n-alkanes Proc. Combust. Inst. 36 (2) (2017) 2531–2539.
[52] U.M. Ascher, L.R. Petzold, Computer Methods for Ordinary Differential Equations and Differential-Algebraic Equations, SIAM, Philadelphia, 1998.
[53] G. Buzzi-Ferraris, Scientific C++: Building Numerical Libraries the Object-Oriented Way, Addison Wesley/Longman, New York, 1993.
[54] G.B. Ferraris, D. Manca, BzzOde: a new C++ class for the solution of stiff and non-stiff ordinary differential equation systems Comput. Chem. Eng. 22 (11) (1998) 1595–1621, http://dx.doi.org/10.1016/S0098-1354(98)00233-6.
[55] K. Brenan, S. Campbell, L. Petzold, Numerical Solution of Initial-Value Problems in Differential-Algebraic Equations, North-Holland, New York, 1989.
[56] D. Manca, G. Buzzi-Ferraris, T. Faravelli, E. Ranzi, Numerical problems in the solution of oxidation and combustion models Combust. Theory Model. 5 (2) (2001) 185–199.
[57] L. Ji, A. Cuoci, A. Frassoldati, M. Mehl, T. Avedisian, K. Seshadri, Experimental and computational investigation of the influence of iso-butanol on autoignition of n-decane and n-heptane in non-premixed flows Proc. Combust. Inst. 39 (2) (2023) 2007–2015.
[58] Y. Wang, A. Cuoci, S. Guo, L. Ji, C.T. Avedisian, K. Seshadri, A. Frassoldati, Experimental and numerical investigation of ester droplet combustion: Application to butyl acetate Proc. Combust. Inst. 39 (2) (2023) 2543–2551.
[59] S. Guo, A. Cuoci, Y. Wang, L. Ji, C.T. Avedisian, K. Seshadri, D. Lopez-Pintor, J.E. Dec, N. DiReda, A. Frassoldati, Combustion characteristics and detailed simulations of surrogates for a Tier II gasoline certification fuel Proc. Combust. Inst. 39 (2) (2023) 2493–2502.
[60] A. Nobili, A. Frassoldati, T. Faravelli, A. Cuoci, Soot formation in combustion of spherically symmetric isolated fuel droplets with different initial diameters Fuel 363 (2024) 130403.
[61] W.A. Sirignano, Fluid Dynamics and Transport of Droplets and Sprays, Cambridge University Press, 2010.
[62] A. Dalili, J.D. Brunson, S. Guo, M. Turello, F. Pizzetti, L. Badiali, C.T. Avedisian, K. Seshadri, A. Cuoci, F.A. Williams, A. Frassoldati, M.C. Hicks, The role of composition in the combustion of n-heptane/iso-butanol mixtures: experiments and detailed modelling Combust. Theory Model. (2020) 1–19, http://dx.doi.org/10.1080/13647830.2020.1800823.
[63] H. Nomura, Y. Ujiie, H.J. Rath, J. Sato, M. Kono, Experimental study on high-pressure droplet evaporation using microgravity conditions Symp. (Int.) Combust. 26 (1) (1996) 1267–1273, http://dx.doi.org/10.1016/S0082-0784(96)80344-4.
[64] E. Cipriano, A. Frassoldati, T. Faravelli, S. Popinet, A. Cuoci, A low-mach volume-of-fluid model for the evaporation of suspended droplets in Buoyancy-driven flows 2024, URL https://hal.science/hal-04580590. working paper or preprint.
[65] E. Ranzi, C. Cavallotti, A. Cuoci, A. Frassoldati, M. Pelucchi, T. Faravelli, New reaction classes in the kinetic modeling of low temperature oxidation of n-alkanes Combust. Flame 162 (5) (2015) 1679–1691, http://dx.doi.org/10.1016/j.combustflame.2014.11.030.
[66] G. Xu, M. Ikegami, S. Honma, K. Ikeda, X. Ma, H. Nagaishi, D. Dietrich, P. Struk, Inverse influence of initial diameter on droplet burning rate in cold and hot ambiences: A thermal action of flame in balance with heat loss Int. J. Heat Mass Transfer 46 (7) (2003) 1155–1169, http://dx.doi.org/10.1016/S0017-9310(02)00397-6.
[67] A. Cuoci, C.T. Avedisian, J.D. Brunson, S. Guo, A. Dalili, Y. Wang, M. Mehl, A. Frassoldati, K. Seshadri, J.E. Dec, et al., Simulating combustion of a seven-component surrogate for a gasoline/ethanol blend including soot formation and comparison with experiments Fuel 288 (2021) 119451.
[68] W. Pejpichestakul, E. Ranzi, M. Pelucchi, A. Frassoldati, A. Cuoci, A. Parente, T. Faravelli, Examination of a soot model in premixed laminar flames at fuel-rich conditions Proc. Combust. Inst. 37 (1) (2019) 1013–1021, http://dx.doi.org/10.1016/j.proci.2018.06.104.
[69] H.G. Weller, G. Tabor, H. Jasak, C. Fureby, A tensorial approach to computational continuum mechanics using object-oriented techniques Comput. Phys. 12 (6) (1998) 620–631.
[70] E. Cipriano, A. Frassoldati, T. Faravelli, S. Popinet, A. Cuoci, et al., Multicomponent droplet evaporation in a geometric volume-of-fluid framework J. Comput. Phys. 507 (2024) 112955.
[71] E. Cipriano, A. Frassoldati, T. Faravelli, S. Popinet, A. Cuoci, A low-mach volume-of-fluid model for the evaporation of suspended droplets in buoyancy-driven flows Int. J. Heat Mass Transfer 234 (2024) 126115, http://dx.doi.org/10.1016/j.ijheatmasstransfer.2024.126115.
[72] E. Cipriano, 2023. http://basilisk.fr/sandbox/ecipriano/.

Alberto Cuoci is a Professor of Chemical Engineering at Politecnico di Milano, working in the numerical modeling of reactive flows including detailed kinetics with a focus on pollutant formation and emissions (NOx, PAHs, and soot). He is the lead developer of OpenSMOKE++, a comprehensive framework for simulating complex chemical reactions. He is currently exploring numerical techniques for accelerating multidimensional CFD simulations with chemical reactions using machine learning algorithms. In addition, he is interested in the multiscale analysis of multiphase flows and catalytic processes.

Edoardo Cipriano is a Ph.D. candidate in Chemical Engineering at Politecnico di Milano, where he also earned his Master's Degree with full marks in the same field. His research focuses on the simulation of multiphase flows, with a particular emphasis on developing numerical methods for phase-changing and reactive systems. Edoardo aims to leverage direct numerical simulations to deepen the understanding of these complex phenomena, guide experimental investigations, and provide valuable insights for simplified engineering models.

Abd Essamade Saufi is a Senior Scientist in the Numerical Physics department at First Light Fusion (Oxford, UK). He works on developing compressible radiation-hydrodynamics codes for simulating plasmas in Inertial Fusion Energy (IFE) applications. He earned his Ph.D. in Chemical Engineering at Politecnico di Milano (2020), defending a thesis on the modeling of the surface tension-driven dynamics, evaporation and gas-phase reactivity of isolated fuel droplets. His interests include numerical methods for compressible hydrodynamics, multi-material flows and reduced-order modeling of IFE targets.

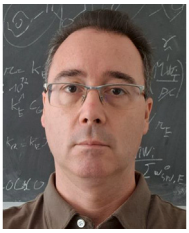

Alessio Frassoldati is a Professor of Chemical Engineering at Politecnico di Milano, renowned for his work in multi-scale modeling of combustion systems, emission reduction, and safety. His research includes developing kinetic mechanisms for fuels ranging from hydrogen to jet fuels, along with advanced CFD modeling of reacting flows. He also investigates NOx chemistry, PAHs, and soot formation. Dr. Frassoldati has authored over 150 journal articles and has played key roles in organizing and reviewing for scientific conferences. He received the 2020 Research Excellence Award and the 2012 Sugden Award from the Combustion Institute.